Journal of Materials Chemistry B

COMMUNICATION

View Article Online
View Journal

Cite this: DOI: 10.1039/d6tb00628k

Received 21st March 2026,
Accepted 22nd May 2026

DOI: 10.1039/d6tb00628k

rsc.li/materials-b

HRP-crosslinked silk–gelatin bioinks: printability dynamics and modulation of stem cell lineage commitment in 3D bioprinted constructs

Chandrashish Roy,† Priya Banerjee† and Sourabh Ghosh *

Advancements in 3D bioprinting demand bioinks that demonstrate not only precise printability and mechanical robustness but also consistent biochemical and cellular performance. From previous iterations in our laboratory, a silk fibroin–gelatin (SF–G) bioink was conjugated with mushroom tyrosinase (MT) as the enzymatic crosslinker. However, its clinical translation was hindered by several limitations, including batch-to-batch variation in concentration and enzymatic activity, protracted gelation kinetics, and inconsistent rheological and structural characteristics. To overcome these challenges, we developed a next-generation SF–G bioink employing horseradish peroxidase (HRP) and hydrogen peroxide (H_2O_2) as an alternative enzymatic crosslinking system. This approach facilitated rapid and tunable crosslinking through β-sheet enhancement, yielding hydrogels with improved stiffness, shape fidelity, and resistance to enzymatic degradation. Detailed rheological analysis confirmed optimal shear-thinning behaviour and print fidelity, while reactive oxygen species (ROS) quantification ensured cytocompatibility across physiologically relevant concentrations. Human bone marrow-derived mesenchymal stem cells (hBMSCs) encapsulated within the constructs maintained high viability and demonstrated robust osteogenic and chondrogenic lineage commitment. Furthermore, supplementation with triiodothyronine (T3) and transforming growth factor-β3 (TGF-β3) augmented matrix deposition and tissue-specific morphogenesis. Notably, a 10 U HRP–H_2O_2 formulation emerged as the most promising candidate, offering a strategic balance of mechanical integrity, bioactivity, and reproducibility. This optimized enzymatic system paves the way for scalable and clinically viable SF–G bioinks tailored for advanced tissue engineering and regenerative medicine applications.

1. Introduction

Three-dimensional (3D) bioprinting has emerged as a cutting-edge approach in tissue engineering, offering the ability to construct complex, cell-laden architectures by precisely depositing biomaterials, living cells, and signalling molecules in a controlled, layer-by-layer manner. Unlike conventional fabrication techniques that often yield oversimplified structures with limited physiological relevance and suboptimal cellular environments, 3D bioprinting enables the re-creation of precise cellular orientation, native tissue architecture and mechanical properties.[1] It has capacity for spatial and temporal control over cell placement, which makes it a powerful platform for engineering anatomically and functionally accurate tissue models *in vitro*.[2] Central to this technology is the use of "bioinks", cell-encapsulating hydrogels, which critically influence cell behavior by providing biochemical and mechanical support.[3] Despite its promise, the development of clinically translatable, structurally robust, and biologically compatible tissue constructs remains a key challenge, largely dependent on the performance and adaptability of the bioink system.[4]

Silk fibroin (SF), a bioink base from *Bombyx mori*, is rich in glycine, alanine, and serine, forming a β-sheet-dominant structure. SF consists of a heavy (≈350 kDa) and light (≈26 kDa) chain with a glycoprotein, P25 (30 kDa), in the ratio of 6 : 6 : 1. A silk biopolymer based bioink can be prepared by controlling the shear force, to induce sol-to-gel transition, due to conversion of the secondary conformations (random coil to β-sheet crystallization).[5] To improve SF's rheology and flow properties, gelatin, a thermo-responsive biopolymer with unique isoelectric characteristics, is blended to create a SF–G composite bioink.[6] This optimized bioink has been successfully utilized in various extrusion-based bioprinting methods, such as the diameter of the extrudate/filament is determined by the nozzle diameter, ink rheology, flow rate and extrusion pressure, crosslinkers.[1] To ensure stability and irreversibility, our laboratory has progressively refined the SF–G bioink for 3D bioprinting employing mushroom tyrosinase (MT) as an enzyme crosslinker, resulting in a uniform formulation appropriate for the engineered bone marrow stromal cell (TVA-BMSC) line, produced using the avian retroviral receptor.[7,8] As a result, various *in vitro* tissue architectures could be reconstructed, as

Regenerative Engineering Laboratory, Department of Textile and Fibre Engineering, Indian Institute of Technology Delhi, New Delhi-110016, India.
E-mail: Sourabh.Ghosh@textile.iitd.ac.in
† Both the authors have contributed equally.

well as to recapitulate embryonic development and creating physiologically relevant *vitro* disease models.[5] For these optimized methods, proper selection of crosslinker is very important.[9] For example, 5SF–15G (5% SF and 15% gelatin) formulation-initiated gelation was induced upon the addition of 500 U of MT crosslinker within 30 min at 28 °C and 15 min at 37 °C. So far in our laboratory, MT was employed as a biocompatible oxidative enzyme to crosslink SF–G bioinks through the oxidation of tyrosine residues, enabling mild gelation conditions suitable for encapsulating viable stem cells within 3D bioprinted constructs.[6] However, at concentrations below 300 U, no gelation was observed even after 1 h of incubation.[7] Despite their effectiveness, MT-based systems often exhibit batch-to-batch variation in enzymatic activity, unavailability, slow and unpredictable gelation kinetics, and inconsistent mechanical and rheological stability. Hence, we need to search for other alternative crosslinking methods.

To overcome these constraints, the current study introduces an alternative cross-linking approach using horseradish peroxidase (HRP) in combination with hydrogen peroxide (H_2O_2). We have explored an HRP/H_2O_2-mediated cross-linking system to achieve faster, tunable, and reproducible gelation with enhanced mechanical uniformity and cytocompatibility.[9] This system enables efficient and rapid gelation at significantly lower enzyme concentrations (*e.g.*, 10–15 U), offering improved consistency, faster kinetics, and greater cost-effectiveness compared to tyrosinase-based crosslinking. HRP, a heme-containing oxidoreductase extracted from *Armoracia rusticana*, catalyzes the oxidation of a broad spectrum of aromatic hydrogen donors *via* free-radical polymerization.[10] Enzymatic cross-linking of SF using the HRP–H_2O_2 system has been previously explored as a mild and cytocompatible strategy for hydrogel formation. In this mechanism, HRP catalyzes the oxidation of phenolic hydroxyl groups of tyrosine residues to form reactive phenoxy radicals, which subsequently undergo radical coupling to generate stable dityrosine covalent cross-links. Earlier studies have demonstrated that this approach enables rapid gelation under physiological conditions while maintaining high biocompatibility and tunable mechanical properties. For instance, McGill *et al.*[11] reported HRP-mediated enzymatic crosslinking of SF hydrogels with controllable gelation kinetics and improved mechanical stability suitable for biomedical applications. Similarly, studies by Marino *et al.*[12] showed that HRP/H_2O_2-mediated silk hydrogel systems provide enhanced structural integrity and cytocompatibility for cell encapsulation.

While these studies established the fundamental enzymatic cross-linking mechanism, their primary focus was on bulk hydrogel formation and biomaterial characterization rather than extrusion-based 3D bioprinting applications. In contrast, the present work extends this principle by integrating HRP/H_2O_2-mediated cross-linking with extrusion-based 3D bioprinting of SF–G bioinks, enabling controlled printability, tunable viscoelastic properties, and directed stem cell lineage commitment within printed constructs.

In SF, which contains approximately 10% tyrosine residues, HRP can facilitate oxidative coupling of phenolic hydroxyl groups to form di-tyrosine covalent crosslinks.[13] This mechanism may offer a more tunable and reproducible enzymatic strategy for hydrogel stabilization and structural integrity enhancement. Kotani *et al.*[14] have demonstrated that HRP-mediated enzymatic crosslinking in the presence of H_2O_2 enables a highly controllable and reproducible hydrogel formation strategy for protein-based bioinks. In this system, HRP catalyzes the oxidation of phenolic moieties, generating phenoxy radicals that undergo covalent coupling to form di-tyrosine crosslinks, thereby stabilizing the hydrogel network. The HRP/H_2O_2 platform supports rapid gelation under mild aqueous conditions, with fine control over cross-linking kinetics and network density achieved by precisely regulating enzyme and peroxide concentrations. Importantly, when H_2O_2 is maintained at low concentrations, efficient cross-link formation can be achieved without inducing oxidative stress, preserving high cytocompatibility. These features render HRP/H_2O_2-mediated cross-linking particularly well suited for stem cell encapsulation and extrusion-based 3D bioprinting applications requiring tunable mechanical integrity and biological fidelity.[14]

Accelerated gelation of SF hydrogels can be achieved by increasing the concentrations of HRP and H_2O_2.[15,16] However, excessive levels of these reagents have been associated with adverse cellular responses, including immunogenicity and cytotoxicity *via* apoptotic or necrotic pathways.[17] The gentle enzymatic cross-linking in water, combined with adjustable mechanical strength, biodegradability, and biocompatibility, makes these silk hydrogels outstanding choices for cell culture and encapsulation.[18,19] Therefore, this study emphasizes the development of a 3D bioprinted construct utilizing low concentrations of HRP and H_2O_2 to preserve cellular viability and function without compromising gel stability.

Although several strategies have been proposed to enable 3D printing of SF-based biomaterials, each approach exhibits distinct advantages and limitations. For instance, salt-bath-assisted printing utilizes ionic cross-linking environments, typically involving potassium phosphate or ammonium sulphate baths, to induce rapid β-sheet formation and structural stabilization of extruded filaments. While this method improves filament integrity during printing, it often requires post-printing immersion steps and diffusion-controlled cross-linking, which may limit spatial control and compatibility with cell-laden constructs.

Alternatively, light-based volumetric or photocross-linking approaches employ photoactive modifications of SF, such as methacrylation, to enable rapid gelation upon exposure to ultraviolet or visible light. These techniques allow high-resolution patterning and rapid fabrication; however, they require chemical modification of the silk backbone and photo-initiators, which may introduce cytotoxicity concerns and alter the intrinsic biophysical properties of the native protein matrix.

In contrast, the HRP/H_2O_2 enzymatic cross-linking strategy presented in this work offers several distinct advantages, including mild aqueous reaction conditions, avoidance of chemical modification of SF, tunable gelation kinetics through

simple enzyme concentration control, and compatibility with cell-laden bioinks. Furthermore, enzymatic cross-linking enables *in situ* gelation during extrusion-based printing, facilitating improved print fidelity and structural stabilization without the need for external irradiation or post-printing chemical treatment. These characteristics highlight the potential of HRP-mediated cross-linking as a clinically translatable and biologically compatible alternative for SF-based bioink systems.

In regenerative medicine, cartilage or bone tissue engineering primarily depends on the chondrogenic or osteogenic differentiation of mesodermal mesenchymal stem cells within porous 3D scaffolds respectively. The articular cartilage in the knee joint is typically sponge-like and has a huge load-bearing capacity. But in cartilage tissue engineering, most of the literature so far report the fabrication of only transient cartilage. Unlike articular cartilage, transient cartilage becomes bone cells and, therefore, brittle within a short time. The immortalized mouse cell line TVA-BMSCs were established using retroviral expression by avian retroviruses with SV40 large T-antigen or we used human turbinate tissue mesenchymal stromal cells derived from nasal inferior turbinate tissues.[20] But human bone marrow derived mesenchymal stem cells might exhibit significant variation in metabolic activity, surface markers and differentiation kinetics than TVA-BMSC or turbinate tissue derived MSC, which would affect chondrogenic outcomes in bioprinting constructs. To have a clinical relevance, instead of using a cell line, we planned to used human BMSc cells.[21]

Members of the transforming growth factor-beta (TGF-β) superfamily, particularly TGF-β3, play a pivotal role in modulating the quality, organization, and biochemical composition of the extracellular matrix (ECM) produced by progenitor cells.[22] Notably, Haider *et al.* reported that TGF-β3 stimulation significantly enhanced the deposition of cartilage- specific ECM components, including collagen type II and aggrecan, within human MSC-laden silk–elastin scaffolds.[1,7] In our laboratory, Chawla *et al.*[7] reported that without TGF-β1 BMSCs encapsulated in a 3D bioprinted SF–G bioink matrix undergo articular cartilage differentiation. On the other hand, triiodothyronine (T3) has emerged as a potent inducer of hypertrophic differentiation in TVA-BMSC aggregates, even at nanomolar concentrations (1 nM).[23] Therefore, this study determines whether HRP–H_2O_2 mediated cross-linking offers faster, more tunable, and reproducible gelation than MT; which cell source, TVA-BMSCs or primary human bone marrow-derived MSCs is most appropriate for clinically relevant tissue engineering; how biochemical cues such as TGF-β3 and triiodothyronine (T3) direct lineage- specific differentiation; and how these parameters collectively influence gene expression and total collagen deposition in 3D bioprinted SF–G constructs. Unlike previously reported MT cross-linked with SF–G hydrogels, which primarily relies on enzymatic oxidation of tyrosine residues with limited control over gelation kinetics, the HRP–H_2O_2 cross-linking system enables rapid and tunable enzymatic cross-linking through controlled variation of HRP and H_2O_2 concentrations. This provides improved regulation of gelation time and viscoelastic properties that are critical for extrusion-based 3D bioprinting. Importantly, the HRP–H_2O_2 system allows modulation of cross-link density and hydrogel microstructure, which directly influences filament stability, printing fidelity, and the cellular microenvironment within the printed constructs. Therefore, this platform represents an advancement over previously reported MT-cross-linked SF–G systems and earlier HRP-crosslinked silk hydrogels that were primarily designed for bulk gel formation rather than bioink optimization for extrusion-based bioprinting applications.

2. Materials and methods

The *Bombyx mori* cocoons were sourced from the Central Silk Board (Bangalore, Ministry of Textiles, Government of India). Lithium bromide (LiBr, Merck), sodium carbonate (Na_2CO_3, Merck), and dialysis cassettes (Merck) were used for extracting the SF solution. Gelatin powder (type A, from porcine skin) was obtained from Merck, mushroom tyrosinase (MT, $\geq$1000 U mg^{-1}) was procured from Sigma-Aldrich, horseradish peroxidase (HRP, 250 U mg^{-1}, type I) was supplied by SRL (Sisco Research Laboratories Pvt. Ltd, Maharashtra, India), and hydrogen peroxide (H_2O_2, 30% w/v) was provided by Thermo Fisher Scientific India Pvt. Ltd. For cell expansion and culture, Dulbecco's modified Eagle's medium (DMEM) low-glucose formulation (Himedia), fetal bovine serum (FBS) (Gibco), penicillin/streptomycin (Gibco), and trypsin/EDTA (Gibco) were used.

2.1. Computational modelling of HRP–H_2O_2 and MT cross-linking in silk fibroin–gelatin

The structure-based virtual screening and computational modelling workflow was designed to elucidate the HRP–H_2O_2 mediated cross-linking mechanism in SF–G systems. Initially, the three-dimensional structures of HRP and H_2O_2 were retrieved from the Protein Data Bank (PDB) and PubChem databases, respectively. The structure of SF, available in the Protein Data Bank (PDB ID: 3UA0), was incorporated into the analysis to model the interaction, particularly, the N-terminal of the silk was used for the enzymatic cross-linking system with the bioink components. Prior to docking, protein structures were subjected to pre-processing and refinement using UCSF Chimera. This included removal of non-standard residues, water molecules, and heteroatoms, followed by the addition of hydrogen atoms and the assignment of Gasteiger charges to optimize the molecular geometry. The prepared ligand structures were also energy-minimized within Chimera to ensure conformational stability before docking. Docking studies were carried out using Autodock Vina.[24] A blind docking approach was employed, in which the entire protein surface was made available as a potential binding site to avoid bias in ligand placement. Multiple docking poses were generated, and each was scored based on binding affinity. The conformation exhibiting the lowest binding energy (c-score) was considered the most favourable and was selected for subsequent validation and analysis. To evaluate structural reliability and interaction

specificity, the docked complexes were visualized and analyzed in PyMOL. Hydrophobic interactions, hydrogen bonding networks, and conformational changes at the binding site were examined in detail. The root-mean-square deviation (RMSD) values were calculated to compare conformational deviations between docked structures, ensuring the stability and reproducibility of the predicted binding mode. The results were further cross-verified using Discovery Studio Visualizer, which provided additional insights into the active site geometry, ligand orientation, and critical non-covalent interactions within the HRP–H_2O_2–SF complex. These analyses were similarly extended to the SF–MT complex to compare enzymatic interaction profiles. This multi-step computational pipeline, combining the strengths of UCSF Chimera (structure preparation and visualization), AutoDock Vina (molecular docking), PyMOL (interaction analysis and RMSD calculations), and Discovery Studio Visualizer (stereochemical validation), ensured high accuracy and reproducibility of the docking results. Collectively, this rigorous *in silico* approach provided mechanistic insights into HRP–H_2O_2 mediated crosslinking interactions with SF–G, as well as SF–MT mediated interactions forming the foundation for understanding enzymatic tunability in the proposed bioink system. To enable a direct comparison between the two enzymatic systems, the same docking workflow was applied to MT (MT; PDB ID: 5M6B). The MT structure was pre-processed identically and docked against SF to evaluate its interaction pattern. For both HRP–H_2O_2 and MT, we calculated the number of hydrogen bonds, the C-score (binding affinity), and the RMSD values to determine docking stability. This allowed us to directly compare which system exhibited a lower (more favourable) C-score and a more stable binding conformation.

2.2. Silk fibroin isolation

SF solution was prepared using a combination of degumming, dissolution, and dialysis as previously discussed.[25] *Bombyx mori* silk cocoons were cut into small pieces and boiled twice in a 0.02 M sodium carbonate (Na_2CO_3) solution for 30 min to remove sericin (degumming). The fibers were then washed several times with deionized water, dried overnight at 37 °C, and dissolved in a 9.3 M lithium bromide (LiBr) solution at 60 °C for 4 h (dissolution). After cooling to room temperature, the solution was dialyzed against deionized water for 48 h to remove LiBr. Centrifugation is performed at 9000 r.p.m. for 20 min to remove impurities. The purified fibroin solution was stored at 4 °C. The final concentration of the SF solution was determined to be 5%.[26]

2.3. Preparation and optimization of the HRP-mediated cross-linked SF–G bioink

The acellular bioink was prepared by incorporating gelatin (6% w/v, 60 mg) into 5% aqueous SF solution and ultrapure water, as explicated previously.[27] To achieve a clear solution, the blended materials (SF–G) were incubated in a thermostatic bath at 37 °C. To initiate enzymatic cross-linking, stock solutions of HRP (10 U μL^{-1}) and H_2O_2 (10 U mL^{-1}) were prepared first. H_2O_2, 30% w/v stock solution was used as the oxidizing agent and diluted to the required working concentration prior to mixing. Equal volumes of HRP solution (10 U μL^{-1}) and diluted H_2O_2 solution were added to 1 mL of the SF–G bioink to initiate enzymatic crosslinking. The final HRP concentrations investigated were 5 U, 10 U, and 15 U as outlined in Table 1.

Table 1 Different concentrations of crosslinker with an equal volume of HRP and H_2O_2 for 1 mL of the SF–G bioink

Sample	HRP concentration (% w/v)	HRP (μL)	H_2O_2 (μL)
SF–G-5 U HRP	5 U	0.5	0.5
SF–G-10 U HRP	10 U	1	1
SF–G-15 U HRP	15 U	1.5	1.5

2.4. Rheological evaluation of bioink properties

The rheological properties of the enzymatically cross-linked SF–G bioink were analysed by assessing viscosity, flow points, and gelation profiles. This was done to verify the printability of the materials and to compare their behavior over time. Measurements were taken in the linear viscoelastic region, where the viscosity is independent of the applied stress or strain. The rheological characterization of 5 U, 10 U, and 15 U HRP cross-linked acellular SF–G bioinks was conducted using an Anton Paar MCR 302 plate-and- plate rheometer at 25 °C, with a 25 mm plate diameter and a gap of 500 μm. The flow behaviour of the enzymatically cross-linked SF–G bioinks under shear stress (Pa) was evaluated by measuring viscosity (Pa s) profiles of the steady-flow solutions against increasing shear rates (s^{-1}) ranging from 0.1 to 10^3, while maintaining environmental conditions.[27] Additionally, an oscillatory amplitude sweep was performed at a fixed frequency of 5 Hz, with strain (%) varying from 0.1 to 10^4, to determine the linear viscoelastic region (LVR) and identify the flow points of the different bioinks, based on the storage modulus (G'), loss modulus (G''), and loss factor. The viscoelastic characteristics of the bioinks were further assessed using an oscillatory frequency sweep test conducted within the LVR, ranging from 0.1 to 100 Hz at a fixed strain of 1%. The gelation kinetics of all cross-linked bioinks were examined through an oscillatory time sweep experiment at a shear strain of 1% and a frequency of 1 Hz. For all formulations, the storage modulus (G') was higher than the loss modulus (G''), indicating the transition from the sol-state to the gel-state.[28] Similarly rheological tests such as shear-thinning behaviour, yield stress analysis, amplitude sweep, frequency sweep and time sweep analysis were performed on SF–G bioinks crosslinked using MT at a concentration of 20 U mL^{-1}. MT initiates gelation by oxidizing tyrosine residues in both SF and gelatin, enabling the formation of dityrosine and amino-quinone crosslinks.

Rheological measurements for MT-crosslinked bioinks were carried out on the same rheometer setup described above (Anton Paar MCR 302, 25 °C, 25 mm plate, 500 μm gap) to ensure direct comparability with the HRP:H_2O_2 system. The viscosity and flow behavior were quantified through steady shear measurements across shear rates ranging from 0.1 to 10^3 s^{-1}, and the materials exhibited shear-thinning behavior

required for printability. Although apparent viscosity values of MT and HRP-cross-linked bioinks were comparable, HRP-cross-linked formulations exhibited superior elastic recovery and structural stability, whereas the 15 U HRP condition showed reduced G' and G'' values, indicating compromised network integrity.

An oscillatory amplitude sweep at 5 Hz with strain increasing from 0.1% to 100% was used to define the LVR and determine the flow point using G', G'', and $\tan\delta$. Viscoelastic profiles were further assessed by a frequency sweep between 0.1 and 100 Hz at 1% strain, providing insight into the elastic and viscous contributions of the tyrosinase-mediated network.

Gelation behavior was examined through an oscillatory time sweep at 1% strain and 1 Hz, enabling continuous monitoring of MT-driven cross-link formation. Similar to HRP:H_2O_2, MT-cross-linked SF–G demonstrated a gradual increase in G', eventually surpassing G''. This confirmed the formation of a stable, elastic hydrogel network through tyrosinase-mediated oxidation and subsequent dityrosine bond formation.

Notably, previously reported tyrosinase-based SF hydrogel systems often employ different cellular models, culture media compositions, and growth factor supplementation strategies, which may significantly influence cellular responses and differentiation outcomes. In the present study, hBMSCs were encapsulated within HRP/H_2O_2-cross-linked SF–G bioinks under controlled culture conditions. Compared with tyrosinase-mediated oxidative coupling, the HRP/H_2O_2 enzymatic system promotes rapid di-tyrosine bond formation, resulting in faster gelation kinetics and enhanced mechanical stability of the printed constructs. These differences in the cross-linking mechanism and scaffold stiffness can substantially influence the microenvironment experienced by encapsulated stem cells and their subsequent lineage commitment.

2.5. Mechanical characterization of cross-linked SF–G hydrogels

The 5 U, 10 U, and 15 U HRP cross-linked SF–G hydrogels (1.5 cm length × 1 cm thickness) were evaluated using an Instron 3365 Universal tester equipped with a 1 kN load cell, operating at a compression rate of 1 mm min^{-1}. The compressive modulus was determined by calculating the slope of the linear region on the stress–strain curve. Non-cross-linked SF and 5 U & 10 U HRP cross-linked SF–G films (4 cm length × 1 cm width) were tested for tensile strength using a Tinius Oslen H5KL Universal tester (ASTM D 882-12 Plastics Tensile Properties of Thin Plastic Sheets) with a 1 kN load cell and a test speed of 20 mm min^{-1}. The film thickness, measured with a digital thickness gauge, was 0.22 mm under a pressure of 39.2×10^{-3} N mm^{-2}.

2.6. Attenuated total reflectance-Fourier transform infrared (ATR-FTIR) analysis of a cross-linked bioink

ATR-FTIR spectra of HRP-cross-linked and non-cross-linked SF–G bioinks were acquired using a NICOLET IS-50 FTIR spectrometer (Thermo Fisher Scientific). A total of 74 scans were recorded per sample at a resolution of 4 cm^{-1} over the 1500–1700 cm^{-1} range to evaluate amide I and amide II band variations associated with enzymatic cross-linking. OriginPro 8.5 (OriginLab Corporation, Northampton, MA, USA) was used for spectral deconvolution.

2.7. Swelling behaviour assessment of hydrogels

The dynamic swelling profile of enzymatically crosslinked SF–G–HRP hydrogels (formulated with 5 U, 10 U, and 15 U HRP per 400 μL of bioink) was systematically evaluated under physiologically relevant isothermal conditions (37 °C) in phosphate-buffered saline (PBS, pH 7.4) over a 15-day period. Initial dry masses (m_{Df}) of the constructs were recorded prior to immersion, and the PBS medium was routinely refreshed to ensure ionic stability and minimize osmotic interference. Swelling kinetics were quantified by gravimetric analysis at predetermined intervals (days 1, 3, 5, 7, 10, and 15) across triplicate samples. The swelling ratio (Q_f) over time was calculated using the following formula:[29] $Q_f = (m_s - m_{Df})/m_{Df} \times 100$, where m_s represents the hydrated mass at each time point. This assessment aimed to elucidate the influence of cross-linking density on the construct's fluid uptake capacity and structural stability in aqueous environments.

2.8. Printability and structural fidelity

Acellular SF–G bioinks were extruded through a 260 μm microcapillary nozzle using a direct write assembly system (Fiber Align, Aerotech Inc., USA) equipped with a pneumatic dispensing unit. Bioinks were loaded into 3 mL syringes, and rheological parameters—including viscosity, yield stress, viscoelasticity, and shear-thinning behavior—were characterized under ambient conditions (21–25 °C) to fine-tune printability.[30,31] Using HRP–H_2O_2 (5 U, 10 U) for *in situ* cross-linking, 1 mL of the bioink was printed (acellular) into single-layered 4 × 4 mm square grids (1.5 mm pore spacing, 6 mm width/height). Printing was performed using a pneumatic extrusion pressure of 20–22 psi, with a printing speed of 1 mm s^{-1} and a layer height of 200 μm. The strand spacing was maintained at 1.5 mm and constructs were allowed to cross-link for approximately 5 min post-printing to achieve structural stabilization. Preliminary constructs enabled comparative evaluation of cross-linked *versus* non-cross-linked SF–G formulations in terms of structural fidelity and extrusion performance using parameters outlined in Table 2. The spreading ratio was calculated as spreading ratio = D_f/D_n, where D_n is the nozzle diameter and D_f is the measured diameter of the extruded filament obtained from optical microscopy images.[32]

The spreading ratio is defined by eqn (1):

$$\text{Spreading ratio} = \text{extruded filament diameter/nozzle's diameter} \quad (1)$$

We also examined the printability index (Pr) and printing accuracy using following eqn (2) and (3):

$$\text{PR} = L^2/16A \quad (2)$$

$$\text{Printing accuracy (\%)} = [1 - (A - A_i)/A_i \times 100] \quad (3)$$

Table 2 Optimized printing parameters for acellular non-crosslinked and crosslinked SF–G bioinks

Sample	Printing temperature	Printing pressure	Printing speed	No. of layers
SF–G	25 °C	15 PSI	1 mm s^{-1}	2
SF–G-5 U HRP	25 °C	20 PSI	1 mm s^{-1}	2
SF–G-10 U HRP	25 °C	22 PSI	1 mm s^{-1}	2

where L is the average perimeter of the pore, A is the average area of the pore and A_i is the designed area of the pore. If Pr = 1 corresponds to perfectly squared pore geometry, Pr < 0026 > 1 corresponds to circular and irregular pore geometry respectively. Values greater than 1 indicate lateral spreading after extrusion.

2.9. Chemiluminescence analysis

Chemiluminescence signal detection was performed using the Bio-Rad ChemiDoc XRS+ gel documentation system. SF–G-10 U HRP–H_2O_2 and SF–G-1000 U HRP–H_2O_2 cross-linked gel matrices were prepared in the presence of luminol, and the resulting chemiluminescence intensity was analyzed to comparatively evaluate the oxidative activity generated during HRP/H_2O_2-mediated enzymatic cross-linking of the SF–G bioink formulations.[33] The assay was specifically performed to assess the relative oxidative environment associated with the gelation process. The imaging system was equipped with a supercooled CCD detector (1392 × 1024 resolution, 4.65 × 4.65 μm pixel size), 16-bit depth (65 535 gray levels), and a dynamic range exceeding 4.0 orders of magnitude. Imaging was conducted in chemiluminescence mode using a special amber emission filter with a spectral range of 548–630 nm. The maximum usable image area was 26 × 35 cm under controlled environmental conditions (21 °C and <70% non-condensing humidity). Following image acquisition, chemiluminescence intensity was quantified using ImageJ software for comparative analysis.

2.10. Formulation of the cell-laden SF–G bioink using hBMSCs

Human bone marrow-derived mesenchymal stem cells (male, 18 years), obtained in accordance with the local ethical committee approval (University Hospital Basel. Prof. Dr Kummer; approval date: 26/03/2007; ref. no. 78/07), were initially expanded up to passage 2. The cells were cultured and expanded up to passage 3 in low-glucose Dulbecco's modified Eagle medium (DMEM), supplemented with 10% fetal bovine serum (FBS), 1% antibiotic–antimycotic solution, and 5 ng mL^{-1} fibroblast growth factor-2 (FGF-2; ProSpec), maintaining cultures at ~80% confluency. Incubation was carried out under standard physiological conditions (37 °C, 5% CO_2, humidified atmosphere), with medium replenished every 48 hours. Before chondrogenic induction, hBMSCs previously expanded to passage 2 were cryopreserved in FBS containing 10% dimethyl sulfoxide (DMSO). We further expanded to passage 3 for all subsequent experiments. To prepare the bioink formulation, 36 mg of sterilized gelatin (6% w/v) was blended with 480 μL of SF solution (5% w/v) to obtain a total volume of 600 μL. The mixture was incubated in a thermostatically controlled water bath at 37 °C for 30 min to ensure homogenous blending and to achieve a clear solution. Following incubation, 60 μL of 10× Dulbecco's modified Eagle medium (DMEM) and 60 μL of 10% fetal bovine serum (FBS) were incorporated into the SF–G solution.[34] Enzymatic cross-linking was initiated by adding HRP and H_2O_2 at a concentration of 10 U per 600 μL of bioink in a 1 : 1 volume ratio.[35] Subsequently, hBMSCs were suspended within the bioink at a density of 1 × 10^5 cells at passage 3 per construct prior to bioprinting. hBMSCs were gently resuspended into the pre-warmed SF–G solution prior to enzymatic activation to avoid premature gelation. HRP and H_2O_2 were added immediately before bioprinting at low concentrations (10 U total), enabling *in situ* cross-linking during and immediately after extrusion, thereby minimizing cellular exposure to reactive intermediates. The total mixing time did not exceed 60 s, and bioprinting was completed within the working window of the bioink.

2.11. Determination of total collagen content

The total collagen content of the cartilage sample was determined by the hydroxyproline assay. Proteinase K-treated samples experienced 18 h of hydrolysis at 120 °C in 12 M HCl. Under a chemical safety cabinet, the construct was then dried for 48 h at 55 °C. The dried mass was reconstituted in H_2O. 100 μl of chloramine T/oxidation buffer mixture was added to each sample and standard, and then incubated at room temperature for 20 min. 100 μl of the diluted dimethylaminobenzaldehyde reagent were added to each sample and standard, and then incubated for 20 min at 60 °C. The absorbance was measured at 560 nm. The readings were corrected by subtracting the blank value. The concentration of hydroxyproline in the samples was determined using the standard curve. The data were modified to represent the dry weight of the cartilage specimens prior to digestion. Reports indicate that collagen comprises 13% hydroxyproline, establishing a ratio of 1 : 7.69 between hydroxyproline and collagen, which served as the basis for estimating collagen concentration.[4] The quantified collagen contents were normalized to DNA content measured using a PicoGreen assay to account for differences in cell number among constructs. Since gelatin is a collagen-derived biomaterial containing hydroxyproline residues, all hydroxyproline analyses in the present study were interpreted as relative comparisons between experimental groups containing identical SF–G compositions and equivalent gelatin concentrations. Therefore, the baseline contribution originating from gelatin-derived hydroxyproline remained consistent across all groups. The comparative analysis was performed between SF–G constructs cultured under matched differentiation conditions, including chondrogenic differentiation medium (CDM) *versus* CDM supplemented with transforming growth factor-beta 3 (TGF-β3), as well as osteogenic differentiation medium (ODM) *versus* ODM supplemented with triiodothyronine (T3).[30]

2.12. Evaluation of osteogenic and chondrogenic differentiation of hBMSC laden 3D bioprinted constructs

To assess lineage-specific differentiation within the 3D microenvironment, hBMSC-laden bioprinted constructs were cultured for 28 days under controlled incubator conditions (37 °C, 5% CO_2, and >95% humidity). Four distinct media formulations were used to induce or maintain chondrogenic and osteogenic phenotypes. Chondrogenic differentiation was evaluated using two groups. The first chondrogenic group (control-2) was maintained in standard chondrogenic medium (CDM), consisting of high-glucose DMEM supplemented with insulin–transferrin–selenium (ITS) premix (6.25 μg mL^{-1} insulin, 6.25 μg mL^{-1} transferrin, 6.25 ng mL^{-1} selenium), 5.33 μg mL^{-1} linoleic acid, 1.25 mg mL^{-1} bovine serum albumin (BSA), 0.1 μM dexamethasone, 37.5 μg mL^{-1} ascorbic acid, 1 mM sodium pyruvate, and antibiotics (100 U mL^{-1} penicillin and 100 μg mL^{-1} streptomycin). The second chondrogenic group received the same CDM supplemented with 10 ng mL^{-1} transforming growth factor-β3 (TGF-β3; Sigma-Aldrich) to induce and enhance chondrogenic differentiation. Also the osteogenic differentiation was evaluated in parallel using two additional groups. The first osteogenic group (control-1) was cultured in standard osteogenic differentiation medium (ODM), composed of high-glucose DMEM supplemented with 10 nM dexamethasone (Dex), 50 μg mL^{-1} ascorbic acid, 10 mM β-glycerophosphate (β-GP), 10% fetal bovine serum (FBS), and 1% penicillin–streptomycin. The second osteogenic group (osteogenic group) received the same ODM supplemented with 1 nM triiodothyronine (T3) to promote enhanced osteogenic differentiation.[31,32] Cells between passages 2 and 4 were used for all experiments to ensure phenotypic stability and reproducibility.

2.13. Gene expression

For quantitative gene expression profiling, hBMSC-laden HRP-crosslinked 3D bioprinted constructs were cultured under chondrogenic (control-2 and CDM + TGF-β3) and osteogenic (control-1 and ODM + T3).

Constructs (n = 3 per group per time point) were collected in 1.5 mL microcentrifuge tubes containing 1 mL of EuroGold RNA Pure reagent (EuroClone, Milano) and immediately snap-frozen in liquid nitrogen, followed by storage at −80 °C until further processing. Prior to RNA isolation, the constructs were enzymatically dissolved using protease treatment to facilitate matrix degradation and release of encapsulated cells, followed by centrifugation to obtain a cell pellet. Total RNA was then extracted from the recovered cell pellet using the Qiagen RNeasy Mini Kit according to the manufacturer's instructions. The concentration and purity of the isolated RNA were assessed spectrophotometrically using a NanoDrop 2000C system (ThermoScientific, USA). Subsequently, 1 μg of total RNA was reverse transcribed into complementary DNA (cDNA) using the SuperScript VILO cDNA Synthesis Kit (Invitrogen, USA) following the supplier's protocol. Quantitative real-time polymerase chain reaction (qRT-PCR) was performed using SYBR Green Master Mix (Qiagen, India) on a Rotor-Gene Q thermocycler (Qiagen, India). Each reaction was run in triplicate in a 25 μL total volume comprising 1 μL cDNA template, 2.5 μL gene-specific primers, and nuclease-free water. Primer sequences for SOX9, COL2A1, NOG, ACAN, RUNX2, COL10A1, MMP13 were designed using Qiagen's QuantiTect Primer Assays or custom-designed and validated prior to use. GAPDH served as the endogenous housekeeping gene for normalization, and 2D monolayer- cultured hBMSCs (day 0) (one is cultured in the absence of osteogenic factors and another is cultured in the absence of chondrogenic factors) were used as the calibrator control for ΔΔCt calculations.[34]

Table 3 List of analysed genes using RT-PCR

Gene	Full gene name
SOX9	SRY-box transcription factor 9
COL2A1	Collagen type II alpha 1 chain
NOG	Noggin
ACAN	Aggrecan
RUNX2	Runt-related transcription factor 2
COL10A1	Collagen type X
MMP13	Matrix metallopeptidase 13
GAPDH	Glyceraldehyde-3-phosphate dehydrogenase (housekeeping)

Relative fold changes in gene expression levels were analyzed using the $2^{-(\Delta\Delta Ct)}$ method, and data processing was carried out using Rotor-Gene Q software (Qiagen). All results were expressed as mean ± standard deviation (SD) from biological triplicates (n = 3). These expression profiles were used to evaluate the temporal progression of osteogenic and chondrogenic markers in different differentiation microenvironments.[35] The list of analyzed genes using is mentioned in Table 3. Primer efficiency was determined using standard curve analysis and ranged between 90% and 110%. Melt-curve analysis was performed following amplification to confirm the presence of a single specific PCR product. Relative gene expression levels were calculated using the $2^{-\Delta\Delta Ct}$ method.

2.14. Statistical analysis

Quantitative data are expressed as mean ± standard deviation (SD). Experiments were performed using three independent biological samples (n = 3), with each measurement conducted in technical triplicate. Statistical analyses were analyzed using one-way ANOVA with GraphPad Prism 8 (GraphPad Software, San Diego, CA, USA). Statistical significance was considered at $p < 0.05$ (*), $p < 0.01$ (**), and $p < 0.001$ (***).

3. Results

3.1. Docking-based evidence of HRP–H_2O_2 mediated SF stabilization in enzymatic cross-linking

The molecular docking analysis was performed to examine the structural compatibility and potential interaction interfaces between SF and the enzymatic components involved in the cross-linking reaction. The computational docking study of the SF–H_2O_2–HRP complex revealed a highly favorable binding configuration, with a predicted binding affinity of

−3.46 kcal mol^{-1} and an exceptionally low RMSD value of 0.01 Å, underscoring both the binding strength and structural reproducibility of the docked model (Fig. 2). The negative binding affinity indicates a strong binding affinity, while the near-zero RMSD value highlights that the conformations obtained are consistent, stable, and energetically favorable. The docking orientation demonstrated that H_2O_2 was precisely localized within the active site pocket of HRP, occupying a catalytically relevant position that is critical for peroxidase activity. The surrounding hydrophobic cavity stabilized the ligand by creating a non-polar environment, while additional polar interactions further reinforced its position. The close packing of H_2O_2 within this cavity ensures accessibility to the catalytic residues of HRP, thereby supporting efficient enzymatic catalysis. SF contributed significantly to the stabilization of the docked complex. The β-sheet domains of SF aligned effectively with HRP's secondary structural elements, promoting van der Waals interactions and structural compatibility. These interactions not only strengthened the binding orientation but also facilitated favourable conformational adjustments that allowed SF to act as a scaffold for H_2O_2 positioning. The visualization confirmed the presence of hydrophobic interaction networks (represented in black in Fig. 2B), which provided additional reinforcement by minimizing solvent exposure of the ligand and stabilizing the binding interface. Importantly, the structural flexibility of SF allowed it to adapt around the HRP–H_2O_2 interface without compromising stability, thereby supporting the formation of a stable enzyme–substrate–substrate complex. This adaptability suggests that the HRP–H_2O_2 system can efficiently induce cross-linking in SF through stable intermediate formation. Collectively, these results validate the molecular compatibility and structural feasibility of the HRP–H_2O_2–SF complex. The favourable docking score, robust interaction network, and negligible RMSD deviation confirm that this enzymatic system is well-suited for mediating cross-linking reactions in SF–G bioinks. The computational evidence thus provides a strong mechanistic basis for the observed tunability and stability of HRP–H_2O_2 mediated crosslinking, supporting its application in developing clinically translatable, structurally robust bioinks. The docking analysis presented here is intended only as a supportive interaction analysis, providing structural insight into possible binding orientations between SF segments and the enzymatic complex. The RMSD value reported by AutoDock Vina corresponds to the lower-bound RMSD between predicted docking poses relative to the best-scoring conformation.

3.2. Gelation and the enzymatic cross-linking mechanism

Controlled gelation kinetics are essential for ensuring optimal printability and stable network formation in SF constructs. HRP–H_2O_2-mediated di-tyrosine cross-linking drives the sol–gel transition; however, excessively rapid gelation can obstruct extrusion, while delayed gelation impairs structural fidelity due to insufficient viscoelastic stabilization.

For the molecular dynamics simulations, the SF sequence used in the model was derived from the repetitive hydrophobic domains of the *Bombyx mori* SF heavy chain. Specifically, the simulation focused on representative segments containing the characteristic glycine–alanine–rich motifs (GAGAGS), which are known to play a critical role in β-sheet formation and structural stability of SF materials. These repetitive sequences are primarily responsible for the mechanical strength and self-assembly behavior of SF. The selected peptide segment therefore serves as a representative model to investigate the intermolecular interactions and structural dynamics relevant to the enzymatic crosslinking process.

To fine-tune enzymatic cross-linking efficiency and ensure irreversible network stabilization, SF–G bioinks were formulated with escalating concentrations of HRP: 5 U, 10 U, and 15 U per mL), while maintaining a stoichiometric ratio of H_2O_2 across all formulations (Fig. 1). The HRP-concentration gradient revealed a dose-dependent acceleration in gelation rate, confirming enhanced cross-linking kinetics with increasing enzyme units. Notably, a comparable study reported gelation within 5 min using 0.2 U HRP per 1 mg of BMSF, reinforcing the role of HRP loading in modulating gelation dynamics.[36]

3.3. Evaluation of SF–G bioinks rheologically

3.3.1. Flow behavior of HRP crosslinked SF–G bioinks. To assess the impact of varying shear rates (ranging from 0.1 to 10^3 s^{-1}) on the viscosity of SF–G bioinks with different concentrations of HRP during the 3D bioprinting process, their rheological behaviour was systematically analysed at 25 °C. This investigation aimed to elucidate the role of enzymatic cross-linking in modulating the flow properties of the bioink formulations. It is well established that a bioink lacking a cross-linker was unsuitable for real-time applications due to the thermo-responsive nature of gelatin, which transitioned to an aqueous phase at physiological temperatures (∼37 °C). Specifically, in the case of the SF–G bioink, gelatin began to liquefy at temperatures exceeding 30 °C. The degumming process significantly affects the molecular weight of regenerated SF as it introduces degradation of the silk polymer chain.[21,37] The steady-state viscosity behaviour of HRP-cross-linked SF–G bioinks as a function of shear rate is illustrated in Fig. 3A. A characteristic shear-thinning response, indicative of non-Newtonian fluid behaviour, was observed across all HRP-crosslinked 5SF–6G bioinks (5 U, 10 U, and 15 U HRP/H_2O_2). As the HRP/H_2O_2 concentration increased (from 5 U to 15 U), the viscosity at lower shear rates was found to increase. For instance, at a shear rate of 10 s^{-1}, the viscosity for the 15 U HRP-cross-linked bioink was recorded as 33 189 mPa s, whereas the 10 U and 5 U formulations exhibited viscosities of 31 623 mPa s and 18 571 mPa s, respectively. This trend indicated that greater enzymatic cross-linking, associated with increased β-sheet content, enhanced viscosity at low shear rates (Fig. 3A). Fig. 3J further compared the viscosity of SF–G bioinks cross-linked using MT at a concentration of 20 U mL^{-1} *versus* HRP. MT-cross-linked bioinks demonstrated only moderate viscosity enhancement—higher than uncross linked SF but substantially lower than HRP-crosslinked systems—reflecting weaker network formation. In contrast, HRP-mediated cross-linking

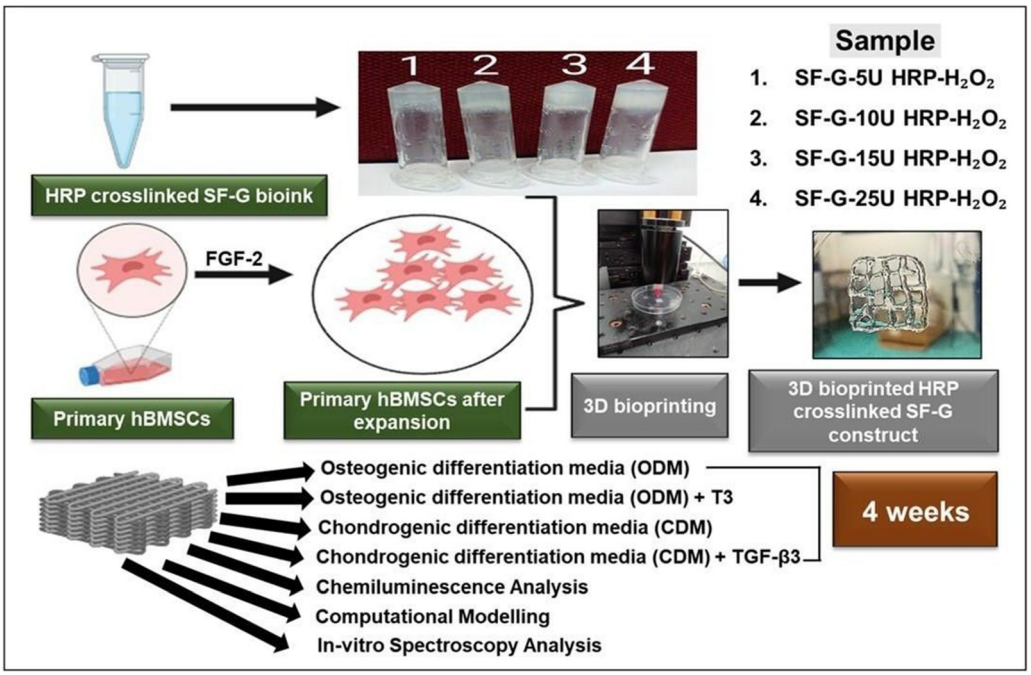

Fig. 1 Schematic overview illustrating the experimental workflow.

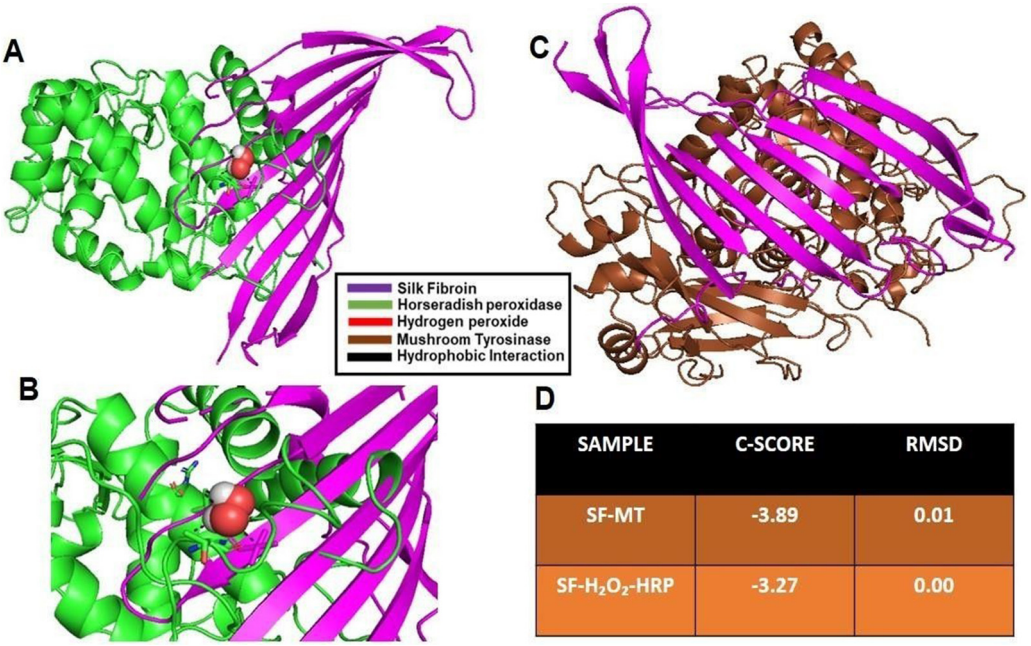

Fig. 2 Computational modelling analysis of the interaction between SF, H_2O_2, HRP and MT. (A) Predicted binding conformation showing SF (magenta), HRP (green), and H_2O_2 (red) at the interface, with black mesh representing hydrophobic interactions. (B) Enlarged view of the binding pocket highlighting the spatial orientation and molecular interactions between H_2O_2 and surrounding residues of SF and HRP. (C) Docking output illustrating the binding conformation of SF with MT, demonstrating favourable interaction stability. (D) Comparative C-score and RMSD values for SF–MT and SF–H_2O_2–HRP complexes, indicating strong binding affinity and high structural reliability for both systems.

produced a significantly stronger and denser polymer network, resulting in higher viscosity retention and more pronounced shear-thinning behaviour across all tested shear rates. Therefore, HRP provided superior rheological performance for extrusion-based bioprinting compared to MT, which generated only partial crosslinking.

The minimum stress required to disrupt the covalently cross-linked network and initiate flow, known as the yield

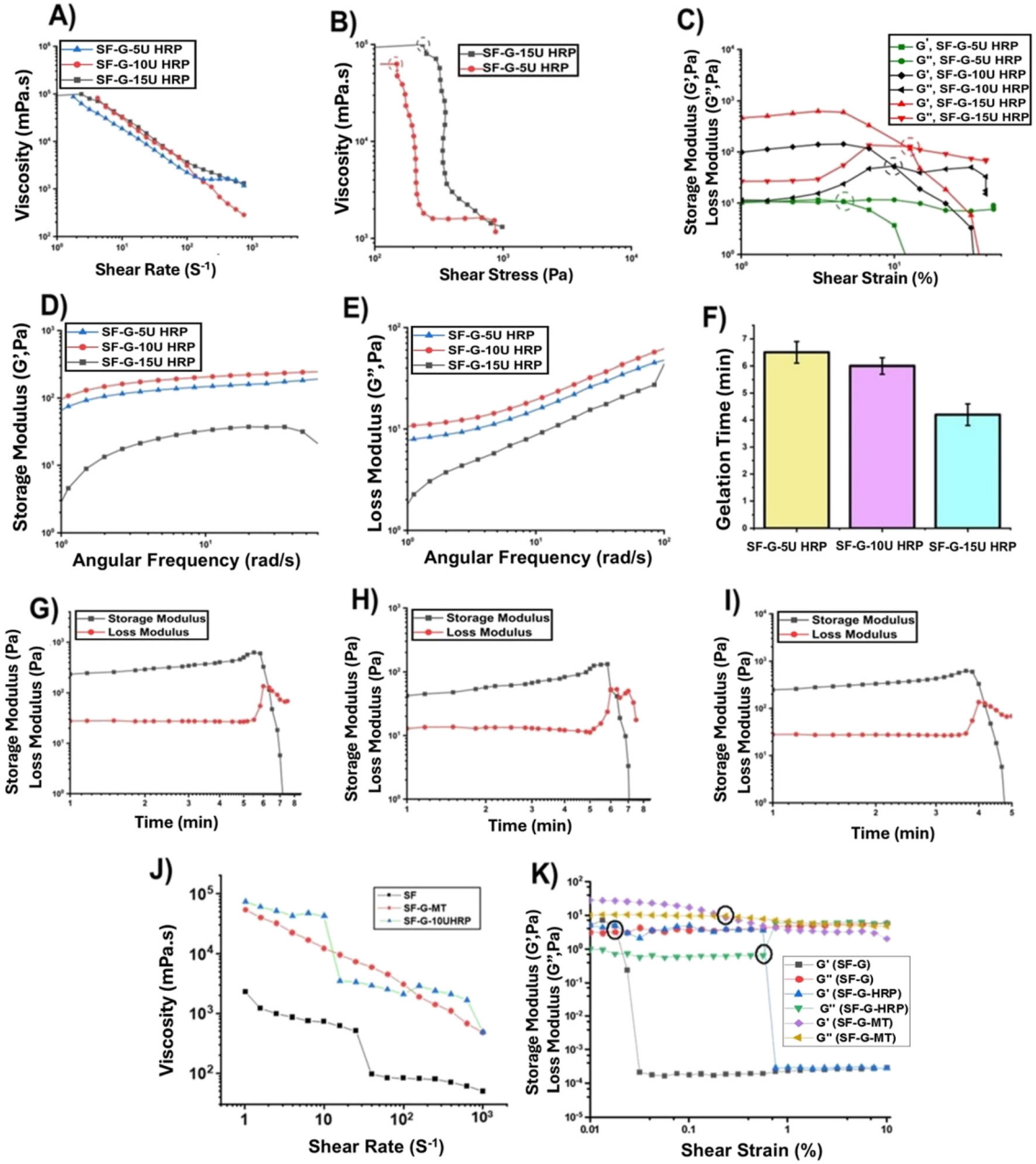

Fig. 3 Rheological characterization of HRP-crosslinked SF–G bioinks, (A) shear-thinning behaviour; (B) yield stress values; (C) amplitude sweep; (D) and (E) frequency sweep; (F) gelation time comparison; (G)–(I) time sweep showing gelation kinetics for 5 U, 10 U, and 15 U HRP–H_2O_2 crosslinked bioinks; (J) viscosity comparison of SF, SF–G–MT, and SF–G-10 U HRP formulations; (K) shear-rate-dependent storage (G') and loss (G'') moduli for MT- and HRP-mediated SF–G bioinks. Data are presented as mean ± standard deviation (SD) from three independent experiments (n = 3). Statistical significance for compressive modulus (*B*) and strain at break (*D*) was determined using one-way ANOVA followed by Tukey's multiple comparison test, with $p < 0.05$ considered statistically significant.

point,[38,39] was determined from the viscosity *versus* shear stress graph (Fig. 3B). The results indicate that yield stress values decrease with a reduction in HRP concentration. Specifically, the yield stress for the highly cross-linked bioink (15 U HRP) was measured at 236.28 Pa, whereas the bioink with the lowest cross-linker concentration (5 U HRP) exhibited a yield stress of 148.76 Pa.

3.3.2. Analysis of oscillatory amplitude and oscillatory frequency sweeps. In oscillatory rheology, gels were subjected to either a frequency sweep, where the oscillation frequency decreased at a constant strain within the linear viscoelastic region (LVR), or a strain sweep, where the oscillatory strain increased at a fixed frequency. The storage modulus (G') represented the energy stored and recovered during each deformation cycle, characterizing the material's solid-like or elastic properties. In contrast, the loss modulus (G'') quantified the dissipated energy, corresponding to the viscous or liquid-like behaviour of the material. The intersection point of G' and

G'', where G'' exceeded G', was defined as the flow point. The interaction between these rheological parameters, particularly within the LVR, provided crucial insights into the sol–gel transition and the viscoelastic characteristics of HRP-crosslinked SF–G bioinks with varying cross-linker concentrations. As depicted in Fig. 3C, the flow point for the highly crosslinked (15 U HRP) acellular bioink occurred at a significantly higher strain (12.7%), whereas bioinks containing 10 U and 5 U HRP exhibited flow points at 10% and 4.66% shear strain, respectively. Higher shear strain was required to disrupt the network structure of highly crosslinked polymer chains, facilitating material flow.[40]

Consequently, optimizing enzymatic cross-linking concentration is essential for fabricating mechanically stable biofabricated tissue-mimicking 3D constructs. A reduction in HRP concentration results in weaker enzymatic cross-linking within the composite hydrogel, leading to the formation of mechanically fragile gels that require minimal shear strain to disrupt their structural integrity.

To prevent sample breakage during testing, a constant shear strain of 1% was applied in subsequent oscillatory frequency sweep experiments. The storage modulus (G') of all cross-linked bioinks exhibited a linear dependence on angular frequency (ω), with a decrease in G' observed as HRP/H_2O_2 concentration was reduced, indicating increased gel softness (Fig. 3D). At an angular frequency of 35.3 rad s^{-1}, the storage moduli of SF–G bioinks containing 5 U, 10 U, and 15 U HRP were 37.25 Pa, 174.61 Pa, and 236.09 Pa, respectively. Softer hydrogels, such as those formed with 5 U HRP, exhibit reduced resistance to deformation and less efficient energy dissipation, resulting in a lower loss modulus (Fig. 3E). Additionally, Fig. 3K evaluates shear-rate-dependent storage (G') and loss (G'') moduli for MT and HRP-crosslinked SF–G systems. MT crosslinking proceeds *via* enzymatic oxidation of phenolic residues into reactive *o*-quinones, which slowly undergo Michael-type addition and Schiff-base reactions, producing a moderately cross-linked network that is highly dependent on dissolved oxygen. This mechanism facilitates smoother extrusion and allows the bioink to tolerate a wider shear range, as reflected in stable G' and G'' across increasing shear rates, but the absolute G' remains relatively low, indicating softer, less densely interconnected hydrogels with limited post-printing stiffness. In contrast, the HRP–H_2O_2 system rapidly generates covalent dityrosine bonds through peroxidase-mediated free radical reactions, forming a highly interconnected and mechanically robust network. Oscillatory strain and frequency sweeps (Fig. 3C–E) show that HRP-crosslinked SF–G bioinks achieve significantly higher G', faster gelation kinetics, and pronounced elastic dominance, while increasing HRP concentration further elevates G' and delays the flow point, demonstrating stronger resistance to deformation. Moreover, HRP-mediated gels maintain higher viscosity and stiffness under increasing shear, enabling superior shape retention immediately after extrusion. Collectively, rheological assessment indicates that while MT provides smoother extrusion and broad shear adaptability, HRP–H_2O_2 produces stiffer, structurally stable constructs with superior post-printing fidelity, making it the technically preferred cross-linking strategy for high-stiffness, durable 3D bioprinted architectures.

3.3.3. Effect of cross-linkers on gelation kinetics of SF–G bioinks. A popular method for monitoring structural evolution and stability as a function of these parameters over a predetermined period of time is time sweep rheology. As a crucial indicator of the gelation kinetics, the gelation point (viscoelastic crossover point) is established when the storage modulus (G') equals the loss modulus (G'').[10] As seen in Fig. 3G–I, G' and G'' increased quickly at first during time sweep studies before stabilizing over longer time scales. The viscoelastic crossover point ($G' = G''$) indicates the transition from liquid-like to solid-like behavior of the bioink. The observed sudden decrease in storage modulus (G') accompanied by a transient increase in loss modulus (G'') around 6 min during the time sweep experiment likely corresponds to a temporary network rearrangement occurring during the enzymatic cross-linking process. At this stage, the developing hydrogel network undergoes structural reorganization as newly generated phenoxy radicals form additional dityrosine bonds. This dynamic restructuring temporarily reduces the elastic dominance of the network, resulting in a momentary decrease in G' and a relative increase in viscous dissipation (G'').

Following this transient rearrangement phase, the continued formation of covalent cross-links stabilizes the polymer network, leading to a subsequent increase in storage modulus and the establishment of a mechanically stable hydrogel. Similar rheological transitions have been reported in enzymatically crosslinked protein hydrogels, where network maturation and crosslink redistribution produce temporary fluctuations in viscoelastic parameters during gelation. As shown in Fig. 3F, the bioink crosslinked with 5 U HRP, for instance, had the prolonged gelation time (6.5 ± 0.4 minutes), while those cross-linked with 15 U and 10 U HRP had shorter gelation times (4.2 ± 0.4 min and 6 ± 0.3 min, respectively). MT-crosslinked samples are included for direct comparison of yield stress behavior across different cross-linking strategies.

3.4. Mechanical stiffness and recovery characteristics under unconfined compression

HRP-incorporated hydrogels were soft and transparent and exhibited significant elasticity. Even when subjected to a 1 kN load during the compression test, these covalently cross-linked SF–G hydrogels showed exceptional elastic recovery and fatigue resistance without any rupture. Under the same stress circumstances, hydrogels with a higher HRP concentration (15 U) showed lower strain percentages than those with lower concentrations (5 U, 10 U), according to the stress–strain analysis (Fig. 4A). By evaluating the tangent of the stress–strain curve at 20% and 40% strain, the compressive modulus was ascertained.[41] As shown in Fig. 4B, the mechanical properties of the hydrogels exhibited a clear quantitative dependence on HRP concentration, indicating that enzymatic cross-link density directly governs network stiffness. As the HRP concentration increased from 5 U to 15 U, the compressive modulus

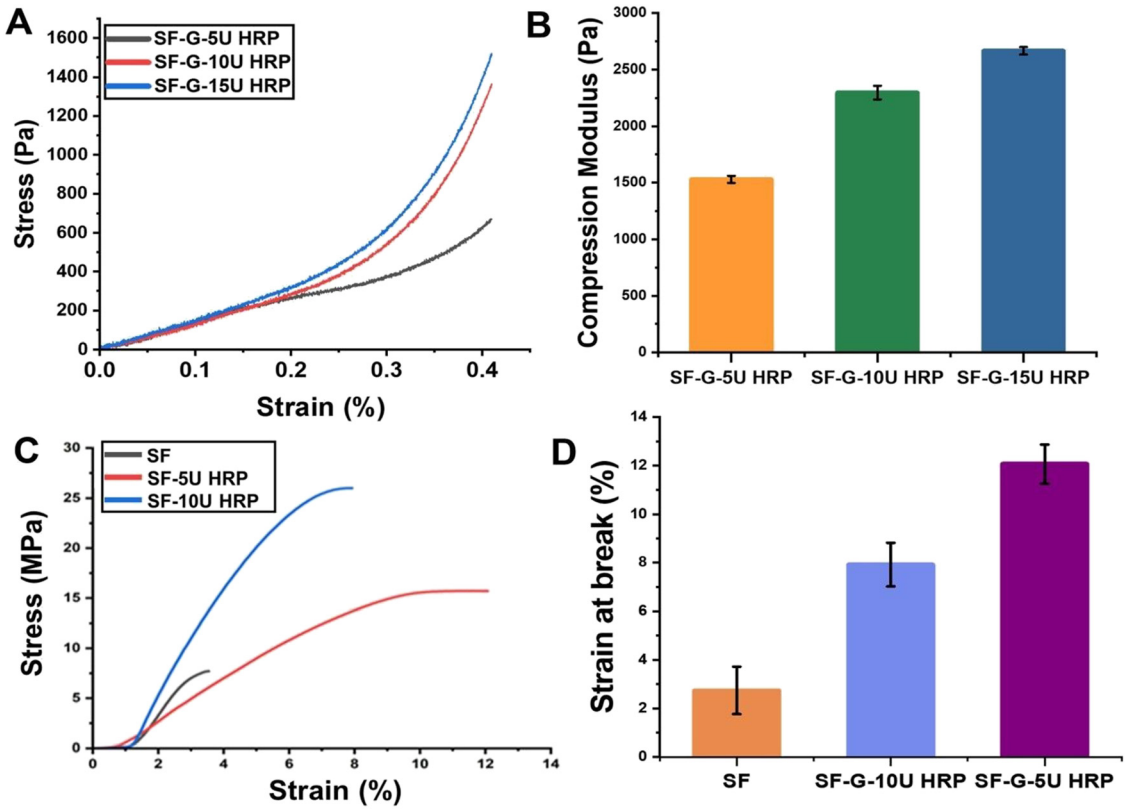

Fig. 4 Mechanical assessment, (A) compressive stress–strain curves of HRP-crosslinked hydrogels; (B) corresponding compressive modulus; (C) tensile stress–strain profiles of non-cross-linked and cross-linked SF films; (D) comparison of breaking strain. Data are presented as mean ± SD (n = 3). Statistical significance for compressive modulus (*B*) and breaking strain (*D*) was determined using one-way ANOVA with Tukey's multiple comparison test ($p < 0.05$).

increased from 1529 ± 31.89 Pa to 2665 ± 4.25 Pa, representing approximately a 74% enhancement in mechanical stiffness. This trend indicates that increasing HRP concentration enhances the formation of dityrosine cross-links, thereby increasing the effective cross-linking density within the SF–G polymer network.

HRP mediated enzymatic cross-linking in the bioink plays a pivotal role in modulating the mechanical integrity of the casted films. This study underscores the intrinsic mechanical limitations of pure SF materials, which present challenges in surgical handling and scaffold implantation. To address these constraints, HRP/H_2O_2-mediated cross-linking of SF–G was employed to enhance the mechanical properties for fabricating mechanically stable biofabricated tissue-mimicking constructs. Tensile strength evaluations revealed that the pure SF film exhibits a lower fracture stress (7.69 ± 1.2 MPa) compared to the HRP-crosslinked variants.

Similarly, tensile testing demonstrated a progressive increase in failure stress with increasing enzymatic cross-linking. As illustrated in Fig. 4C, the tensile strength increased from 15.6 ± 1.1 MPa for SF–G-5 U HRP films to 26.01 ± 0.7 MPa for SF–G-10 U HRP films, corresponding to an approximately 67% increase in tensile load-bearing capacity. This improvement in mechanical performance can be attributed to enhanced intermolecular coupling between tyrosine residues within the SF matrix, leading to improved load transfer across the hydrogel network. These results confirm that HRP concentration serves as a tunable parameter to modulate mechanical stiffness and structural integrity of the printed constructs, which is essential for tailoring bioink properties for specific tissue engineering applications.

Notably, an increase in cross-linker concentration correlates with an improvement in tensile strength, thereby augmenting the material's ability to endure higher mechanical loads.[42] Furthermore, pure SF films fracture at a strain of 2.74 ± 0.979%. In contrast, the SF–G-5 U HRP film, characterized by greater extensibility, exhibits a higher strain at break (12.066 ± 0.8%) compared to the SF–G-10 U HRP film, which breaks at a strain of 7.923 ± 0.9%, as depicted in Fig. 4D. MT-cross-linked bioinks exhibited a moderate increase in viscosity relative to non-cross-linked SF–G; however, HRP-cross-linked systems demonstrated enhanced elastic dominance and network integrity, as reflected in the rheological trends own (Fig. 3J).

The enhanced compressive modulus and tensile properties observed in the HRP-cross-linked SF–G hydrogels, together with the favorable rheological behavior, excellent filament fidelity, and post-printing shape retention, collectively demonstrate the mechanical robustness of the developed printed constructs. The increase in HRP concentration promoted the formation of a more stable cross-linked network, resulting in improved resistance to compressive deformation and enhanced structural

integrity. Furthermore, the shear-thinning and rapid recovery characteristics of the bioink facilitated uniform filament extrusion and maintenance of the printed architecture following deposition. This indicates that the HRP-mediated enzymatic cross-linking contributes significantly to both the mechanical stability as well as the printability of the SF–G bioink system.

3.5. ATR-FTIR analysis of the cross-linked bioink

A reduced peak intensity at 803 cm^{-1} in the SF–G control indicates a lower aromatic content compared to the cross-linked variants. The C–O stretching band, originally at 1060 cm^{-1}, shifted progressively to 1068 cm^{-1} and 1072 cm^{-1} in the 5 U and 10 U HRP-crosslinked samples, respectively (Fig. 5A), suggesting increased molecular ordering and network formation. The FTIR absorption bands in the range of 1637–1616 cm^{-1} correspond to β-sheet structures, while those between 1655–1638 cm^{-1} indicate random coil conformations.[43,44] In the amide I region, a downshift to ~1620 cm^{-1} and an increase in peak area in the cross-linked samples indicated conformational transitions toward β-sheet enrichment. This enrichment was quantified by deconvolution of the amide I region, showing an approximate increase of 25–30% in β-sheet content for 5 U HRP and 35–40% for 10 U HRP-cross-linked samples compared to the uncross-linked control (Fig. 5C and D). A concurrent shift in the amide II band to 1531 cm^{-1} further confirmed this structural reorganization, while minor shifts in the amide III region to 1230 cm^{-1} (5 U) and 1238 cm^{-1} (10 U) were observed, consistent with a more ordered secondary structure within the hydrogel matrix. These results demonstrate that HRP–H_2O_2 cross-linking provides rapid and tunable formation of SF–G hydrogels, where β-sheet enhancement directly contributes to improved mechanical stability and post-printing structural fidelity. The β-sheet enrichment in HRP-crosslinked hydrogels was quantified by deconvoluting the amide I FTIR region (1600–1700 cm^{-1}). Peaks corresponding to β-sheets (1616–1637 cm^{-1}) were separated from random coils and other structures using Gaussian fitting, and the area under the β-sheet peaks was expressed as a percentage of the total amide I area. This analysis showed a 25–30% increase for 5 U HRP and 35–40% for 10 U HRP, correlating directly with enhanced gel stiffness, faster gelation, and improved structural fidelity.

The increase in β-sheet content observed following HRP–H_2O_2-mediated enzymatic cross-linking may be attributed to enzymatically induced molecular stabilization and conformational rearrangement of SF chains. In the presence of H_2O_2, HRP catalyzes the oxidation of tyrosine residues present in SF–G, generating phenoxy radicals that subsequently form

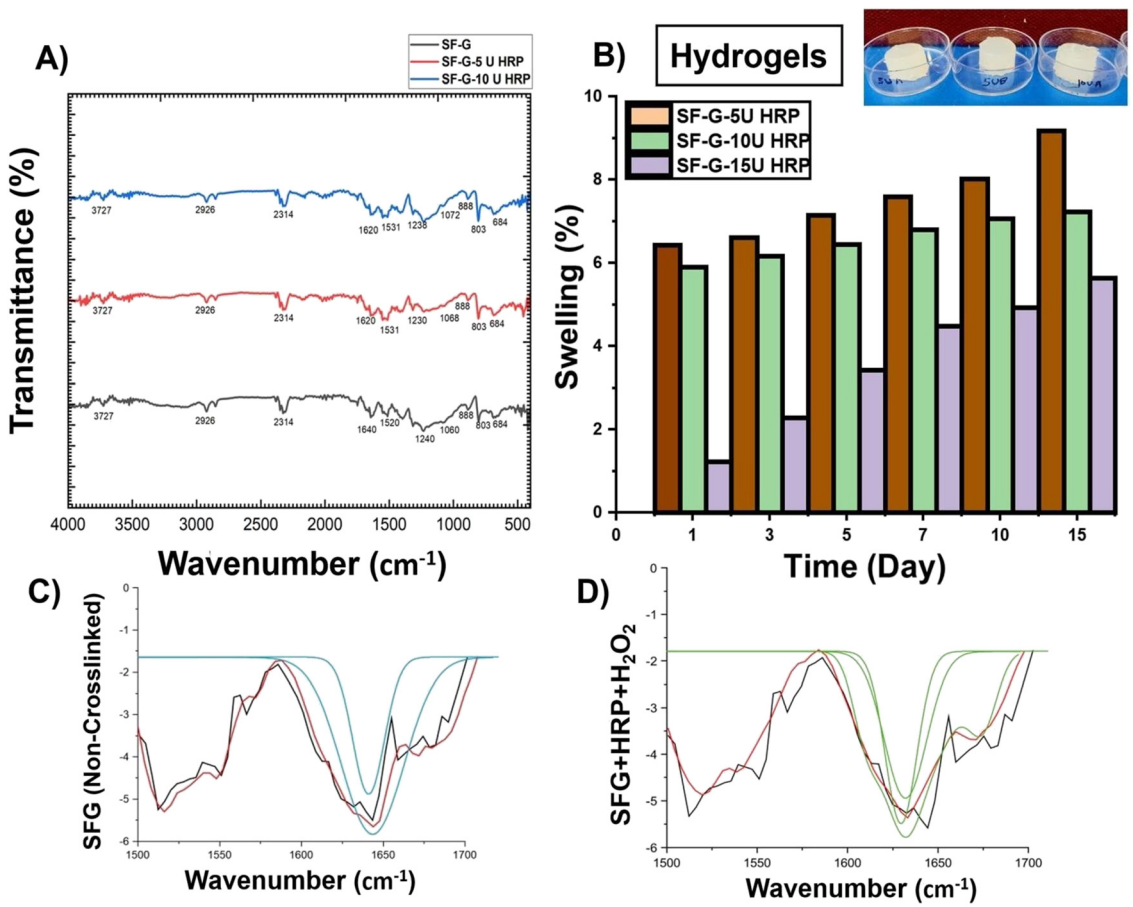

Fig. 5 (A) ATR-FTIR spectra of non-crosslinked and HRP-crosslinked SF–G hydrogels; (B) swelling behavior (%) over 15 days; (C) and (D) amide I region deconvolution (1590–1710 cm^{-1}) illustrating secondary structural transitions of noncrosslinked and HRP crosslinked SF–G samples. Data are presented as mean ± SD. Statistical significance for swelling behaviour (B) was determined using one-way ANOVA with Tukey's multiple comparison test ($p < 0.05$).

intermolecular dityrosine covalent cross-links within the hydrogel network. The formation of these covalent cross-links restricts polymer chain mobility and promotes closer molecular packing, intermolecular hydrogen bonding, and alignment of SF chains. Such molecular rearrangement facilitates the transition from random coil/silk I conformations toward more thermodynamically stable β-sheet-rich silk II structures. The enhanced β-sheet formation increases the crystalline character of the hydrogel network, thereby contributing to improved structural rigidity, mechanical stability, and resistance to dissolution.

3.6. Enzymatic stability of crosslinked SF–G hydrogels

SF–G hydrogels exhibit substantial swelling over a 15-day period in PBS solution (Fig. 5B). Over time, the swelling gradually slows until the hydrogels reach saturation. In hydrogel systems with higher HRP concentrations, the swelling progression (Q_f) is slower due to the formation of denser and more robust physical networks, resulting in markedly lower swelling values. For instance, the hydrogels cross-linked with 5, 10, and 15 U HRP demonstrate swelling percentages of 9.17%, 7.23%, and 5.63%, respectively, over 15 days. These differences highlight the impact of HRP concentration on the cross-link density and network integrity. However, hydrogels with higher swelling ratios are less stable, as excessive water uptake can weaken the hydrogel structure, reducing its mechanical integrity and longevity.

3.7. Optimization of filament formation and shape fidelity

The printability of bioinks was evaluated in terms of shape fidelity within the *x*–*y* plane by quantifying key parameters such as the spreading ratio, printability index (Pr), and printing accuracy.[44] Consequently, the utilization of low-concentration cross-linkers is recommended to enhance bioink performance. In this study, we sought to achieve optimal printability of hydrogels by employing minimal concentrations of HRP as a cross-linking agent. Extrusion-based bioprinting bioinks generally exhibit shear-thinning behaviour, wherein elevated nozzle velocities reduce viscosity and subsequently increase surface tension.[45] The ideal spreading ratio, indicated by the ratio between the nozzle diameter and extruded filament diameter should approximate unity (1.0) to ensure accurate construct formation. To mitigate fluctuations across experimental trials, various strategies were implemented to enhance printability and minimize bioink spreading. Specifically, extrusion pressure should be maintained at a nearly constant level to ensure uniform filament deposition.[46] A 260 μm nozzle was utilized for all print trials. Optical images of bioprinted constructs were analyzed *via* ImageJ software to quantify filament diameter, perimeter, and the area of interconnected channels, (Fig. 6B and D).

Quantitative assessment revealed that the spreading ratio of non-crosslinked SF–G bioink was 2.52 ± 0.047, whereas SF–G bioinks cross-linked with 5 U and 15 U HRP/H_2O_2 exhibited spreading ratios of 2.03 ± 0.055 and 1.57 ± 0.042, respectively (Fig. 6A). For an ideal gelation state or near-perfect printability, the interconnected pores should exhibit a square morphology. Deviations from this geometry indicate suboptimal gelation, often attributed to low viscosity or nonideal cross-linking conditions, which can cause filament coalescence and reduced shape fidelity. The printability index (Pr), which provides a relative evaluation of pore geometry, further substantiated these findings. Non-crosslinked SF–G bioink exhibited a Pr value of 0.8 (< 1), indicative of a circular pore architecture, whereas cross-linked SF–G bioinks (5 U and 10 U HRP) demonstrated Pr values of 1.096 and 1.066, respectively, suggesting the formation of near-square geometries (Fig. 6C). Furthermore, printing accuracy assessments revealed that the non-crosslinked SF–G bioink achieved an accuracy of 75.17 ± 4.61%, while the cross-linked SF–G bioinks with 5 U and 10 U HRP exhibited improved accuracies of 77.52 ± 2.14% and 82.97 ± 4.04%, respectively (Fig. 6E). These findings underscore the significance of enzymatic cross-linking in augmenting filament stability during extrusion, as the viscosity of SF–G bioink was observed to increase proportionally with cross-linker concentration. Based on the printability optimization results, the SF–G bioink cross-linked with 10 U HRP exhibited superior shape fidelity, printing accuracy, and pore geometry compared to 5 U and 15 U HRP crosslinker concentrations. Therefore, this optimized formulation (10 U HRP) was selected for further biological evaluation. For the cellular compatibility and functional performance, cells were subsequently embedded within the SF–G-10 U HRP bioprinted constructs. Fig. 6F illustrates the distribution and spreading of cells within the printed constructs, indicating that the bioink matrix supports cell attachment and maintenance of cell morphology. These observations confirm that the optimized SF–G-10 U HRP bioink not only provides enhanced printability but also supports a favorable microenvironment for cell encapsulation and post-printing differentiation.

3.8. Chemiluminescence analysis

The chemiluminescence response observed in the SF–HRP–luminol system demonstrates a substantial enhancement upon the inclusion of hydrogen peroxide (H_2O_2), a crucial oxidizing agent that drives the luminescent reaction. The HRP enzyme catalyzes the oxidation of luminol in the presence of H_2O_2, leading to the formation of an excited-state 3-aminophthalate ion.[47] Upon returning to its ground state, this ion emits visible light, with peak emission typically centered around 548–630 nm as shown in Fig. 7. The HRP-mediated cross-linking reaction exhibited pronounced H_2O_2 sensitivity, as evidenced by a luminescence enhancement exceeding two orders of magnitude in the 1000 U HRP–H_2O_2 formulation compared to the 10 U counterpart, underscoring the catalytic amplification effect of elevated H_2O_2 concentrations. The lower concentration of H_2O_2 and HRP (10 U) cannot sustain the oxidative conditions required for efficient luminol excitation, leading to significantly diminished signal output. This is consistent with prior studies, which establish the essential role of H_2O_2 in enabling the chemiluminescent reaction and in stabilizing the luminescent output, particularly in HRP–luminol systems without additional enhancers. The reduced chemiluminescence intensity observed in

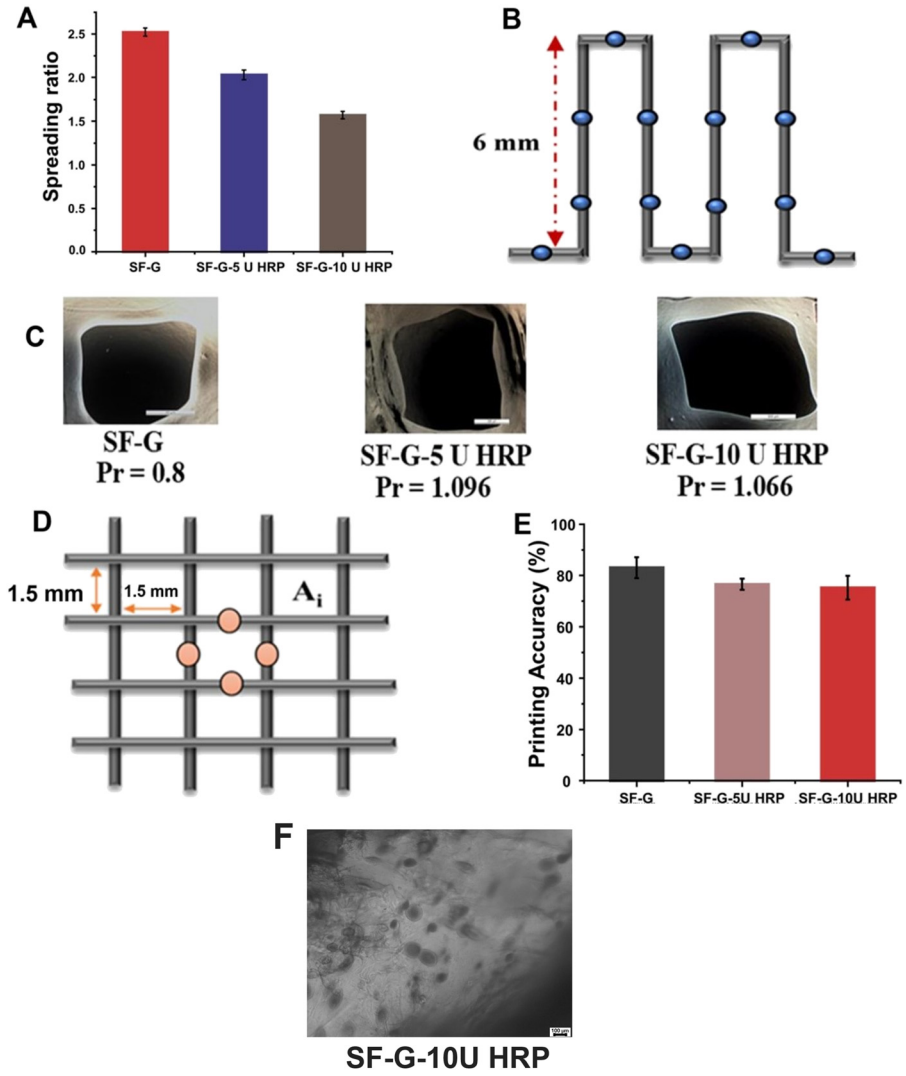

Fig. 6 Printability assessment of SF–G bioinks, (A) spreading ratio; (B) schematic of filament diameter; (C) microscopic pore morphology (scale bar: 500 μm); (D) pore geometry illustration; (E) printing accuracy analysis. (F) Representative microscopic image of cell-laden SF–G-10 U HRP bioprinted construct after 7 days of culture, demonstrating successful cell embedding and division within the enzymatically crosslinked bioprinted construct (scale bar: 100 μm). Data are presented as mean ± SD (n = 3). Statistical significance for spreading ratio (*A*) and printing accuracy (*E*) was determined using one-way ANOVA with Tukey's multiple comparison test ($p < 0.05$).

the HRP/H_2O_2-cross-linked system suggests a lower level of oxidative reaction during the crosslinking process. The results, quantified using ImageJ from Bio-Rad ChemiDoc XRS+ gel images, confirm that the luminol–HRP–H_2O_2 interaction embedded within a SF matrix exhibits robust light emission and underscores the viability of this configuration for bioanalytical applications, particularly where enzymatically triggered chemiluminescence is desired.

3.9. Gene expression analysis

The RT-qPCR analysis was performed on 3D bioprinted SF–G bioprinted constructs encapsulating hBMSCs to investigate the temporal dynamics of lineage-specific gene expression in two defined differentiation microenvironments: chondrogenic differentiation medium supplemented with transforming growth factor-β3 (CDM + TGF-β3) and osteogenic differentiation medium supplemented with triiodothyronine (ODM + T3). Glyceraldehyde-3-phosphate dehydrogenase (GAPDH) was used as the housekeeping reference gene to normalize expression values across all time points. Gene expression was monitored over a 28-day period at four critical stages—days 7, 14, 21, and 28—corresponding to early lineage induction, mid-phase progression, late differentiation, and prolonged matrix maturation.

3.10. Chondrogenic differentiation (CDM + TGF-β3)

Under chondrogenic conditions, the transcriptional profile revealed a progressive and coordinated upregulation of key cartilage-specific genes, confirming effective chondrogenic induction and maintenance of a non-hypertrophic phenotype. SOX9, the central transcription factor driving chondrocyte lineage commitment and regulating extracellular matrix synthesis,

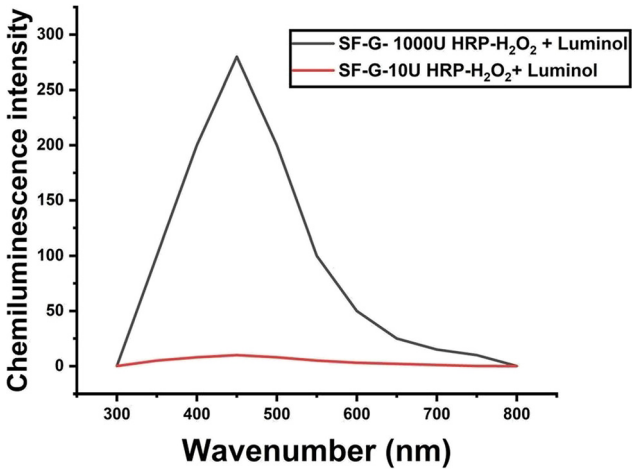

Fig. 7 Chemiluminescence intensity detected within the emission wavelength window of 548–630 nm.

demonstrated a steady increase across all time points. Expression rose from ~2.76-fold on day 7 (1.49 in CDM *vs.* 0.54 in control), increased to ~6.6-fold by day 14 (2.704/0.41), peaked at ~6.7-fold on day 21 (3.35/0.50), and remained elevated at ~7.4-fold on day 28 (3.7/0.5). This persistent activation underscores the essential role of SOX9 in maintaining chondrocyte identity during matrix deposition and maturation. COL2A1, encoding type II collagen, showed a pronounced and sustained upregulation. It was induced by ~4.64-fold at day 7 (1.81/0.39), increased to ~7.22-fold at day 14 (3.61/0.50), reached a dramatic peak of ~22-fold at day 21 (13/0.59), and maintained high expression at ~20-fold by day 28 (12/0.6). This robust induction indicates active synthesis of a cartilage-specific collagen matrix, characteristic of a maturing chondrogenic phenotype. NOG (Noggin), a known antagonist of bone morphogenetic protein (BMP) signaling that prevents hypertrophic differentiation and ossification, showed early activation and sustained expression throughout the culture period. It was upregulated by ~2.93-fold at day 7 (3.51/1.2), remained moderately expressed at day 14 (~1.23-fold), surged again to ~5.58-fold at day 21 (2.79/0.5), and was maintained at ~5.2-fold on day 28 (2.6/0.5). The persistent upregulation of NOG highlights its critical role in suppressing hypertrophy and preserving the articular cartilage phenotype. ACAN (aggrecan), the major cartilage proteoglycan responsible for osmotic swelling and compressive strength, exhibited substantial early induction with a ~21.8-fold increase at day 7 (3.49/0.16), followed by ~7.24-fold at day 14 (7.1/0.98), and stabilized at ~3.79-fold and ~3.6-fold at days 21 and 28, respectively (3.79/1; 3.6/1). This temporal expression pattern reflects active ECM accumulation during early differentiation and gradual stabilization during later stages. Collectively, the upregulation of SOX9, COL2A1, ACAN, and NOG under chondrogenic conditions demonstrates a coordinated transcriptional program favoring stable hyaline cartilage formation, characterized by robust ECM deposition and persistent anti-hypertrophic signaling. These results indicate that CDM + TGF-β3 creates a microenvironment that supports the development of a functional articular cartilage-like tissue (see Fig. 8A).

3.11. Osteogenic differentiation (ODM + T3)

The hBMSCs cultured in ODM + T3 exhibited a transcriptional profile consistent with osteoblast differentiation, matrix mineralization, and hypertrophic remodeling. RUNX2, the master transcription factor for osteogenesis, displayed an early and pronounced ~11.9-fold induction at day 7 (4.75/0.4), which declined progressively to ~10-fold at day 14 (2/0.2), ~4.74-fold at day 21 (1.185/0.25), and ~2.83-fold at day 28 (0.85/0.3). This temporal decline indicates a transient yet strong activation of osteogenic programming during the initial phase, followed by attenuation as the matrix matured. ALPL (alkaline phosphatase), essential for mineral deposition, showed the highest expression at day 7 (~12.2-fold; 4.76/0.39), which declined to ~4.5-fold at day 14 (1.89/0.42) and further reduced to ~2-fold and ~1.37-fold at days 21 and 28, respectively (1.8/0.9; 1.1/0.8). COL10A1, encoding type X collagen—the main structural protein in bone—was highly expressed early (~9.46-fold at day 7; 4.73/0.5), maintained at ~3.75-fold at day 14 (3/0.8), reduced to ~1.5-fold at day 21 (1.5/1), and approached baseline (~1.25-fold) by day 28 (1/0.8). BGLAP (Osteocalcin), a late-stage osteoblast marker associated with mineralization, demonstrated a gradual increase, starting with ~1.5-fold induction at day 7 (1.2/0.8), rising to ~2.67-fold at day 14 (2.4/0.9), peaking at ~3.75-fold at day 21 (3/0.8) and stabilizing at ~3.1-fold at day 28 (3.1/1).

This gene expression cascade indicates that ODM + T3 promotes early osteogenic activation *via* RUNX2 and ALPL, followed by a transition toward osteoblast maturation and mineralized matrix formation.

3.12. Total collagen quantification in hBMSC-laden constructs

The total collagen content was quantified to assess the extracellular matrix deposition in hBMSC-laden constructs cultured under chondrogenic (CDM, CDM + TGF-β3) and osteogenic (ODM, ODM + T3) conditions over a period of seven days (Fig. 9A and B). Under chondrogenic conditions (Fig. 9A) collagen content showed a progressive increase from day 1 to day 7 in both the groups, with a consistently higher accumulation in the presence of TGF-β3. On day 1, collagen levels were relatively low, with CDM + TGF-β3 showing slightly higher content (~300 ng) compared to CDM (~250 ng). By day 3, a significant increase was observed in both groups, with CDM + TGF-β3 reaching approximately 680 ng, surpassing CDM (~500 ng). On day 5, collagen content in both groups continued to rise, showing similar levels (~940 ng in CDM + TGF-β3 *vs.* ~900 ng in CDM). However, by day 7, the difference became more evident, with CDM + TGF-β3 achieving a markedly higher collagen deposition (~1350 ng) compared to CDM (~1100 ng), highlighting the pronounced effect of TGF-β3 in sustaining collagen synthesis during chondrogenesis. A similar trend was observed under osteogenic conditions (Fig. 6B), where collagen content increased gradually over time, with ODM + T3

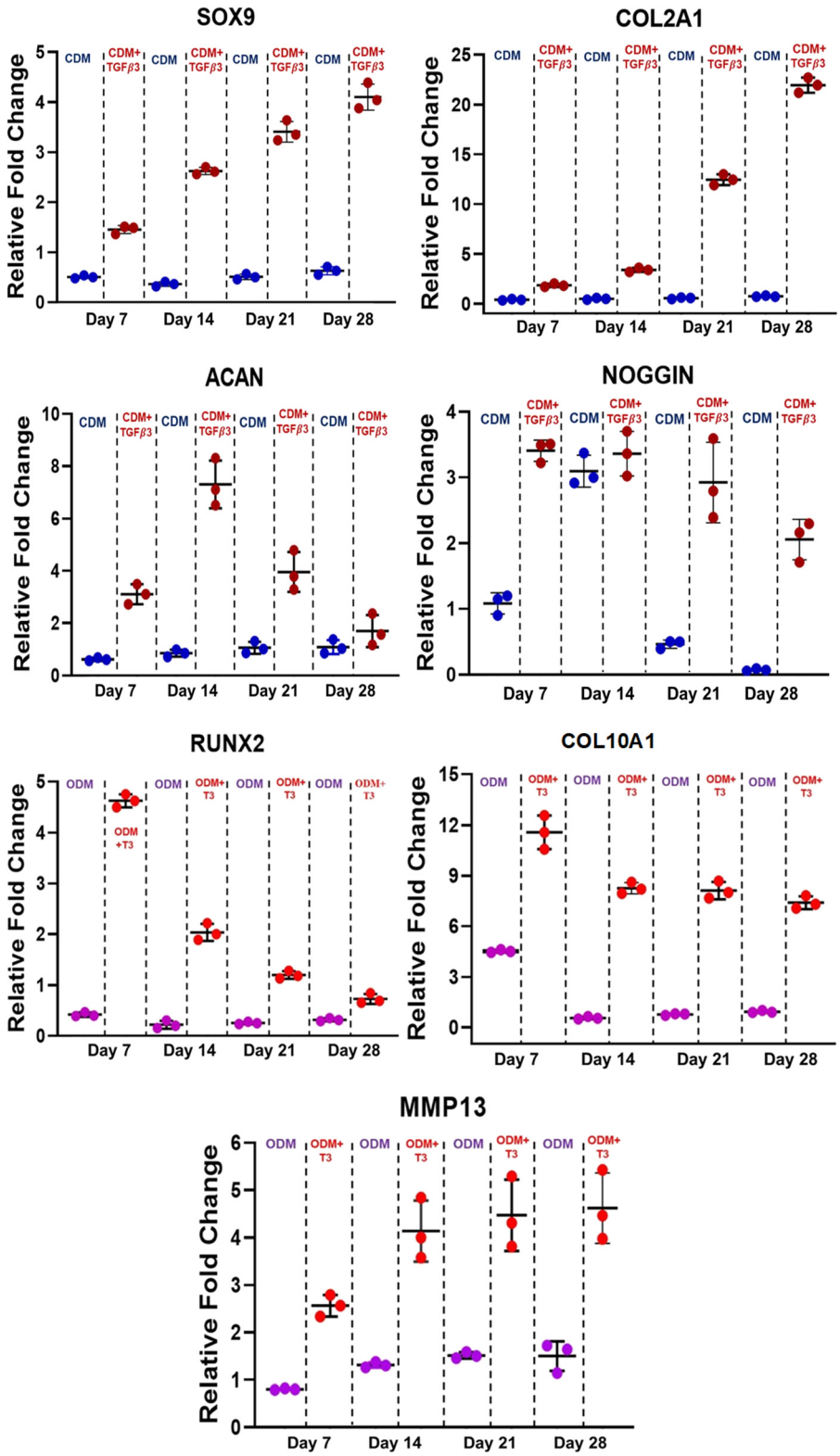

Fig. 8 qRT–PCR analysis of gene expression in hBMSC-laden 3D bioprinted constructs, showing the relative expression of SOX9, COL2A1, NOG, ACAN, RUNX2, COL10A1, and MMP13 under chondrogenic conditions (CDM and CDM + TGF-β_3) and osteogenic conditions (ODM and ODM + T_3) over a 28-day culture period. Relative fold changes were calculated using the $2^{-\Delta\Delta Ct}$ method, with monolayer hBMSCs at day 0 used as the control. Data are presented as mean ± SD (n = 3). Statistical significance was determined using two-way ANOVA with Tukey's multiple comparison test ($p < 0.05$).

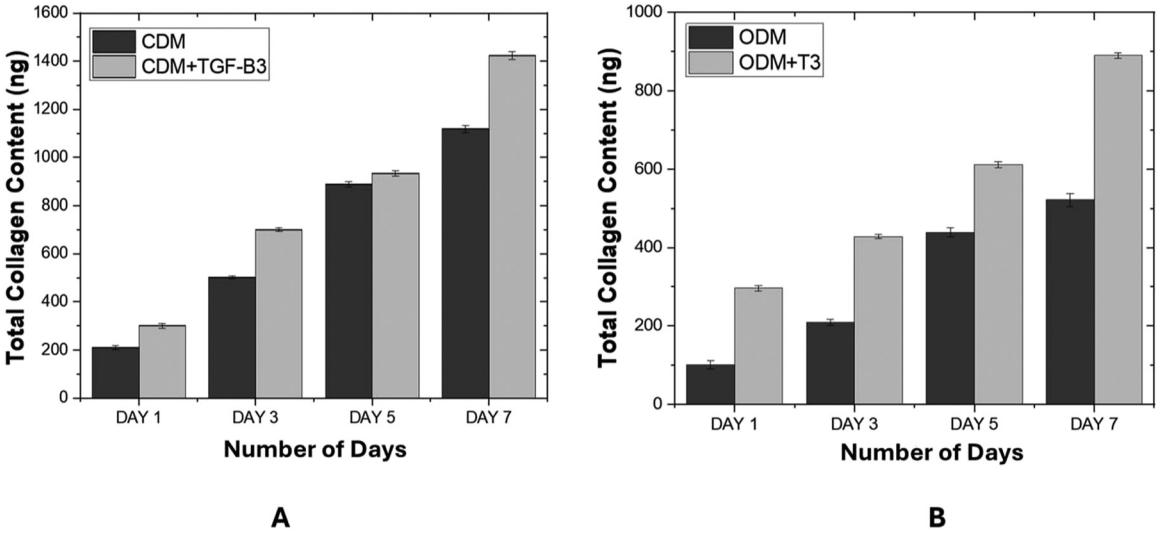

Fig. 9 Total collagen content in hBMSC-laden constructs cultured under chondrogenic and osteogenic conditions over 7 days. (A) Collagen deposition under chondrogenic medium (CDM) and CDM supplemented with TGF-β3, showing a progressive increase with enhanced accumulation in the TGF-β3 group. (B) Collagen deposition under osteogenic medium (ODM) and ODM supplemented with T3, indicating a time-dependent increase with higher collagen levels in the T3-treated group. Data are presented as mean ± SD (n = 3). Statistical significance for (A) and (B) was determined using two-way ANOVA with Tukey's multiple comparison test ($p < 0.05$).

consistently demonstrating higher levels than ODM alone. On day 1, the ODM + T3 group exhibited significantly greater collagen content (~300 ng) compared to ODM (~100 ng), indicating an early stimulatory influence of T3 on collagen synthesis. This difference persisted through day 3 (~420 ng *vs.* ~200 ng) and day 5 (~600 ng *vs.* ~450 ng) and became more pronounced by day 7, where ODM + T3 reached nearly ~900 ng, while ODM remained lower at ~520 ng. The results demonstrated a clear time-dependent increase in collagen deposition in both chondrogenic and osteogenic lineages, with growth factor supplementation (TGF-β3 in CDM and T3 in ODM) significantly enhancing collagen synthesis compared to their respective controls. By the end of the culture period, chondrogenic constructs, particularly those treated with TGF-β3, exhibited a higher absolute collagen content than osteogenic constructs, reflecting their superior matrix synthesis potential under these conditions. The observed differences in hydroxyproline content between the SF–G + CDM and SF–G + CDM + TGF-β3 groups, as well as between the SF–G + ODM and SF–G + ODM + T3 groups, are primarily attributed to differences in cell-mediated extracellular matrix synthesis under the respective differentiation conditions. Since all experimental groups were prepared using identical SF–G bioink compositions containing equivalent gelatin concentrations, the baseline contribution originating from gelatin-derived hydroxyproline remained constant within each comparative group.

3.13. Comparative pathway regulation and differentiation outcomes

The 28-day temporal gene expression analysis conducted on the 3D bioprinted SF–G hydrogel constructs revealed two distinctly regulated lineage trajectories under different inductive conditions, highlighting the platform's versatility in directing mesenchymal stem cell fate. Under osteogenic induction medium supplemented with triiodothyronine (ODM + T3), the Wnt/β-catenin signalling pathway was notably activated, initiating a cascade of molecular events that drive transient cartilage formation, chondrocyte hypertrophy, and subsequent endochondral ossification. This lineage commitment was characterized by an early upregulation of RUNX2, a master transcription factor for osteogenic differentiation, followed by increased expression of matrix remodeling enzymes such as MMP13, which facilitate extracellular matrix degradation and remodeling. Over the course of the culture period, this early molecular profile transitioned toward the expression of key osteogenic markers, including COL10A1 and BGLAP, along with elevated ALPL activity, collectively indicative of osteoblast maturation and matrix mineralization, making this pathway particularly relevant for engineering osteochondral interfaces or bone–cartilage transitional zones.

Chondrogenic induction using medium supplemented with TGF-β3 (CDM + TGF-β3) engaged an entirely different signaling axis, wherein Wnt/β-catenin activity was actively suppressed while the autotaxin–lysophosphatidic acid (ATX–LPA) pathway was prominently activated. This regulatory mechanism played a crucial role in maintaining a stable chondrogenic phenotype by sustaining SOX9 expression, a pivotal transcription factor for chondrocyte lineage commitment and cartilage-specific ECM production. Moreover, this pathway promoted the upregulation of NOG, a known antagonist of BMP signalling, thereby inhibiting hypertrophic progression and preventing premature mineralization. The chondrogenic lineage was further characterized by robust and sustained synthesis of articular cartilage-specific ECM components, including COL2A1 (type II collagen) and ACAN (aggrecan), alongside persistent NOG-mediated suppression of hypertrophic markers, ultimately supporting the

formation of a stable, non-hypertrophic articular cartilage-like tissue suitable for long-term cartilage repair and regeneration.

4. Discussion

The development of clinically translatable, mechanically robust, and biologically instructive bioinks is a critical challenge in cartilage and osteochondral tissue engineering. In this study, we investigated the performance of HRP–H_2O_2–cross-linked SF–G bioinks for supporting lineage-specific differentiation of hBMSCs. Previous work in our lab involved encapsulation of the SF–G bioink with immortalized cell lines, TVA-BMSC, or human turbinate tissue derived MSC, which were engineered to express specifically targeted transcription factors or different differential kinetics, as reported by Chawla *et al.* [7] and Das *et al.*[20] MT has also been shown to effectively cross-link SF–G when combined with Fe_3O_4 magnetic nanoparticles as reported by Chakraborty *et al.*[48] Even in the presence of 50 mg mL^{-1} of MNPs, MT provided efficient crosslinking and supported chondrogenesis and cell viability for up to 21 days in culture. In the present study, we emphasize the need to transition from MT to HRP–H_2O_2 as a crosslinking agent, reflecting a broader advancement in enzymatic biofabrication toward faster, tunable, and clinically scalable cross-linking mechanisms suitable for cell-laden bioprinting.

In the earlier work, MT served as an oxidative biocatalyst to promote dityrosine bond formation within SF–G hydrogels under mild, cytocompatible conditions, providing an alternative to UV or chemical cross-linking that preserved cell viability during 3D bioprinting. Despite its biocompatibility and its ability to activate osteogenic differentiation, the MT-based system presented several limitations. Gelation kinetics were slow and inconsistent (typically 15–30 min under physiological conditions), resulting in delayed construct stabilization and reduced layer fidelity during deposition. Moreover, high enzyme concentrations ($\geq$300–500 U) were required to achieve adequate cross-link density, which not only increased cost but also introduced batch-to-batch variability in mechanical and rheological properties. MT-crosslinked scaffolds exhibited excessive swelling ($>$10%) and premature relaxation of the polymeric network, leading to reduced shape retention and early degradation—factors detrimental to load-bearing or long-term *in vitro* culture. Additionally, the limited commercial availability and rising cost of MT further compromise its feasibility for large-scale or GMP-compliant biofabrication.[49]

In contrast, the HRP–H_2O_2 cross-linking strategy developed in this study achieved rapid and controllable gelation (4–6 min) with a significantly lower enzyme concentration (10 U HRP), representing a $\sim$30–50-fold reduction in enzymatic load compared to MT. The tunable oxidative kinetics of HRP enabled precise regulation of gelation and superior print fidelity (printability index $\approx$ 1.06; accuracy $\approx$ 82.9%), ensuring stable layer-by-layer deposition without pore collapse. Rheologically, HRP-cross-linked SF–G bioinks exhibited pronounced shear-thinning behavior and an optimal viscosity ($\sim$31 600 mPa s at 10 s^{-1}), conducive to smooth extrusion and structural maintenance. The 10 U HRP formulation displayed a compressive modulus of $\sim$2.29 kPa and fracture stress of $\sim$26 MPa—both significantly higher than MT-cross-linked analogs—indicating improved network uniformity and β-sheet ordering, corroborated by the amide I band shift ($\sim$1620 cm^{-1}) in ATR–FTIR spectra. Controlled swelling (5.6–7.2%) and enhanced resistance to hydrolytic degradation further highlight the structural stability of HRP–H_2O_2 networks, whereas MT-cross-linked scaffolds from earlier studies exhibited higher swelling and loss of integrity over comparable time frames. HRP–H_2O_2 enables rapid and controllable gelation (4–6 min) at low enzyme concentration (10 U) as compared to MT which requires the gelation times of (15–30 min) and much higher enzyme loading, leading to variability in print fidelity and mechanical stability. The HRP–H_2O_2 system operates under controlled and transient oxidative conditions, where H_2O_2 is rapidly consumed during cross-linking minimizes prolonged ROS exposure preserving cell viability and supporting stable lineage-specific differentiation. Beyond the biomaterial advantages, the biological comparison between the present HRP–H_2O_2 system and the previously published MT-based work by Chawla *et al.*[7] highlights fundamental differences in cellular responses, lineage stability, and growth factor dependency. Chawla *et al.*[7] employed TVA-BMSCs, a genetically engineered mouse mesenchymal cell line modified to express the TVA receptor for viral transduction. These cells were encapsulated in MT-crosslinked SF–G scaffolds, where MT served as the oxidative enzyme enabling dityrosine bond formation. Their study focused on examining how TGF-β1 regulates cartilage phenotype within this MT-based microenvironment. In the absence of TGF-β1, TVA-BMSCs displayed an articular cartilage-like gene expression profile, characterized by elevated ACAN, PRG4, and ATX, along with suppression of hypertrophic markers such as COL-II (embryonic/transient form), IHH, and COL-X. This indicated a stable hyaline-like state when MT constructs were cultured without exogenous growth factors. However, upon addition of TGF-β1, Chawla *et al.*[7] observed a clear hypertrophic shift. RT-PCR results showed significant upregulation of COL-II, IHH, and COL-X, coupled with downregulation of articular markers (ACAN, PRG4). Their conclusion was clear: TGF-β1 drives TVA-BMSCs toward a hypertrophic, transient-cartilage phenotype, and avoiding hypertrophy in their system required complete withdrawal of TGF-β1. The primary hBMSCs represent the most clinically relevant and translationally appropriate cell source as compared to TVA-BMSCs which are genetically engineered murine cells optimized for mechanistic studies, while turbinate-derived MSCs show tissue-specific and donor-dependent variability. In contrast, hBMSCs possess well-defined differentiation trajectories and are widely accepted for cartilage and bone tissue engineering applications.

The present study utilizes hBMSCs—a clinically relevant, non-engineered human cell population with well-defined differentiation trajectories. These cells were encapsulated in HRP–H_2O_2–cross-linked SF–G constructs, which provide a

mechanically uniform, oxidation-controlled, low-ROS microenvironment fundamentally different from MT-crosslinked gels. While TVA-BMSCs became hypertrophic in response to TGF-β1, hBMSCs continued normal chondrogenic differentiation under TGF-β3 without signs of hypertrophy. RT-PCR analyses in our system revealed strong and progressive upregulation of SOX9, ACAN, COL2A1, and NOG, with minimal expression of hypertrophic markers such as COL-X and MMP13, even at later time points. This indicates that TGF-β3 in HRP-cross-linked constructs promotes a stable hyaline phenotype without triggering the hypertrophic cascade commonly associated with TGF-β1. Moreover, the combination of higher mechanical integrity, faster and more homogeneous crosslinking, lower swelling, and improved β-sheet stabilization in HRP–H_2O_2 hydrogels likely contributes to enhanced cartilage-specific lineage stabilization by improving cell–matrix mechanotransduction and reducing oxidative stress. Altogether, these findings demonstrate that the HRP–H_2O_2 + TGF-β3 environment is biologically superior to the MT + TGF-β1 system for maintaining non-hypertrophic hyaline cartilage in hBMSCs.

In addition to differences with the MT-based TVA-BMSC model, it is also necessary to compare our osteogenic findings using MT as the cross-linker for the SF–G bioink but with an entirely different biological design.[24] Majumder *et al.*'s[24] objective was to chemically conjugate small-molecule regulators (LDN193189, IL-1Ra) and TGF-β3 to the silk backbone using CyCl and diazonium chemistries, enabling sustained release and high local bioavailability to maintain a stable chondrogenic phenotype and suppress hypertrophic maturation in hBMSCs under OA-mimicking conditions. Their gene expression analysis therefore focused on chondrogenic markers (SOX9, PRG-4, and COL2A1) and hypertrophic/catabolic markers (COL10A1, MMP13, NOG, and SMAD4). As expected, the IL-1Ra group showed the lowest MMP-13 and COL10A1, while the LDN and TGF-β3 groups showed donor-dependent hypertrophic gene upregulation. This confirmed that their system was engineered to inhibit MMP-13, limit hypertrophic progression, and stabilize the cartilage matrix. Importantly, their constructs did not induce osteogenic markers such as RUNX2 (osteogenic form) or COL10A1, because their design goal was chondrogenic stability, not osteogenesis.[24]

Our HRP–H_2O_2–cross-linked SF–G constructs supplemented with T3 were specifically designed to promote endochondral osteogenesis and therefore exhibited a fundamentally different transcriptional profile. In our study, hBMSCs demonstrated a clear temporal induction of RUNX2 beginning at day 14 and increasing through day 28, indicating osteoprogenitor activation, whereas Majumdar *et al.*[35] maintained low RUNX2 to avoid hypertrophic drift. COL10A1 expressions in our system increased sharply from day 7 onward, confirming active osteoblast-mediated extracellular matrix deposition, a behaviour not observed in Majumder's *et al.*'s MT-based cartilage-stabilization system. Moreover, MMP13 in our constructs increased under T3 conditions, particularly at days 14 and 21, consistent with physiological matrix remodelling during osteoblast maturation. This contrasts directly with Majumdar *et al.*,[35] where MMP-13 was intentionally suppressed (especially in the IL-1Ra group) to prevent hypertrophy and maintain a stable cartilage phenotype. TGF-β3 promotes stable chondrogenesis in HRP-crosslinked constructs, while T3 specifically drives controlled osteogenic progression, enabling stage-dependent lineage control.

Taken together, the gene-specific comparison shows that Majumdar *et al.*'s[24] MT- cross-linked, inhibitor-functionalized system is optimized to reduce MMP-13, restrain COL10A1, and avoid RUNX2/COL10A1 induction, thereby stabilizing chondrogenesis under OA-like conditions. Conversely, our HRP–H_2O_2 + T3 system is optimized to increase RUNX2, elevate COL10A1, and permit controlled MMP-13 activity, driving a stepwise osteogenic differentiation pathway. These contrasting transcriptional outcomes arise from both the distinct biological objectives (hypertrophy inhibition *vs.* osteogenesis) and the differences in cross-linking chemistry (slow MT-based gelation *vs.* rapid, uniform HRP–H_2O_2 network formation). Therefore, while Majumdar *et al.*[35] successfully established a strategy for stabilizing hyaline cartilage phenotype, our system supports full early-to-intermediate osteogenic progression, representing a fundamentally different regenerative pathway. Another study by Kotani *et al.*[13] primarily evaluated the cytocompatibility of HRP-mediated extrusion bioprinting at the cellular level by assessing post-printing cell viability, morphology, and proliferation. Their study demonstrated high survival (>90%) of mouse fibroblasts (10T1/2) and sustained growth and spheroid formation of HepG2 cells within HRP-crosslinked constructs, confirming that the HRP–H_2O_2 system supports basic cell maintenance and proliferation in low-viscosity bioinks. However, the cellular analysis in their work was limited to viability and growth behavior, without investigation of lineage commitment or differentiation-associated gene expression. In contrast, our study extends the cellular evaluation to lineage-specific differentiation of hBMSCs within HRP–H_2O_2–crosslinked SF–G constructs. Beyond maintaining high cell viability, we demonstrate controlled regulation of transcriptional programs, including stable chondrogenic gene expression (SOX9, ACAN, COL2A1, and NOG) under TGF-β3 stimulation and temporally regulated induction of osteogenic markers (RUNX2, COL10A1, and MMP13) under T3 treatment. This highlights the ability of the HRP–H_2O_2 microenvironment to support not only cell survival but also programmed stem cell fate decisions, which were not addressed in the earlier study. HRP–H_2O_2–cross-linked constructs under TGF-β3 exhibited cartilage-specific gene expression with dominance of COL2A1 and stable ECM accumulation. Under T3 stimulation, hBMSCs showed temporally regulated induction of RUNX2, increased COL10A1 expression, and controlled MMP13 activity, resulting in enhanced total collagen deposition associated with osteoblast-mediated matrix formation. Overall, the HRP–H_2O_2 enzymatic system addresses the critical biochemical, mechanical, and translational shortcomings inherent in MT-based crosslinking. It enables rapid gelation, lower enzyme dependence, superior mechanical robustness, enhanced β-sheet stabilization, controlled swelling, and higher biological performance, all while

offering better reproducibility and scalability. Importantly, given the increasing scarcity and cost of MT, HRP–H_2O_2 represents a more sustainable and clinically translatable alternative. The enhanced chondrogenic performance observed in the HRP-crosslinked SF–G constructs is likely associated with the combined effects of enzymatic network stabilization, β-sheet enrichment, and improved cell–material interactions. HRP-mediated dityrosine crosslinking increased the structural integrity and mechanical stability of the hydrogel network, as evidenced by the enhanced compressive modulus, tensile behavior, and post-printing shape retention. Simultaneously, the increased β-sheet content contributed to a more stable and organized microenvironment that supported prolonged structural maintenance during *in vitro* culture. Such mechanically stable matrices are known to influence stem cell behavior by regulating cell–matrix interactions and cytoskeletal organization, thereby promoting lineage-specific differentiation. Furthermore, the gelatin component within the SF–G bioink provided bioactive adhesive domains that facilitated cellular attachment and extracellular matrix deposition. The synergistic effects of improved matrix stability, favorable viscoelastic properties, and enhanced cell–material interactions may therefore have contributed to the increased collagen deposition, and upregulated chondrogenic differentiation observed in the HRP-crosslinked constructs. Thus, the present findings establish HRP–H_2O_2–mediated cross-linking as a next-generation enzymatic approach that overcomes the limitations of the MT system, marking a significant step toward reproducible, functional, and clinically relevant 3D bioprinted constructs for cartilage, bone, and osteochondral tissue engineering.

5. Conclusion

This study highlights the critical role of HRP–H_2O_2 enzymatic cross-linking in fine- tuning the printability, mechanics, and biological performance of SF–G bioinks. Among tested concentrations, 10 U HRP emerged as the optimal cross-linker, balancing rapid yet controlled gelation, enhanced viscoelasticity, and superior mechanical strength without excessive stiffness seen at 15 U. ATR-FTIR confirmed favourable β-sheet structuring at 10 U, while swelling tests demonstrated reduced network degradation, supporting long-term stability. Importantly, 10 U HRP bioinks exhibited improved filament fidelity and print accuracy, coupled with significantly lower ROS generation compared to higher enzyme levels, ensuring a non-cytotoxic environment ideal for stem cell viability. Gene expression analysis further confirmed that SF–G constructs cross-linked at 10 U robustly support hBMSC differentiation, promoting stable chondrogenic and osteogenic lineage commitment depending on induction cues. Overall, the SF–G-10 U HRP–H_2O_2 system offers a precisely tuned, biocompatible platform that synergizes mechanical robustness with controlled cellular microenvironments, positioning it as a versatile biomaterial for advanced 3D bioprinting and tissue engineering applications.

Conflicts of interest

The authors declare that they have no known competing financial interests or personal relationships that could have appeared to influence the work reported in this paper.

Data availability

The data will be available with the corresponding author on reasonable request.

References

1 S. Chawla, S. Midha, A. Sharma and S. Ghosh, Silk-Based Bioinks for 3D Bioprinting, *Adv. Healthcare Mater.*, 2018, **7**(8), 1701204, DOI: 10.1002/adhm.201701204.
2 D. Trucco, A. Sharma, C. Manferdini, E. Gabusi, M. Petretta, G. Desando, L. Ricotti, J. Chakraborty, S. Ghosh and G. Lisignoli, Modeling and Fabrication of Silk Fibroin–Gelatin-Based Constructs Using Extrusion-Based Three-Dimensional Bioprinting, *ACS Biomater. Sci. Eng.*, 2021, **7**(7), 3306–3320, DOI: 10.1021/acsbiomaterials.1c00410.
3 J. Chakraborty and S. Ghosh, Cellular proliferation, self-assembly, and modulation of signaling pathways in silk fibroin gelatin-based 3D bioprinted constructs, *ACS Appl. Bio Mater.*, 2020, **3**(12), 8309–8320, DOI: 10.1021/acsabm.0c01252.
4 J. Chakraborty, J. Fernández-Pérez, K. A. van Kampen, S. Roy, T. Ten Brink, C. Mota and L. Moroni, Development of a biomimetic arch-like 3D bioprinted construct for cartilage regeneration using gelatin methacryloyl and silk fibroin-gelatin bioinks, *Biofabrication*, 2023, **15**(3), 035009, DOI: 10.1088/1758-5090/acc68f.
5 S. Ghosh, S. T. Parker, X. Wang, D. L. Kaplan and J. A. Lewis, Direct-Write Assembly of Microperiodic Silk Fibroin Scaffolds for Tissue Engineering Applications, *Adv. Funct. Mater.*, 2008, **18**(13), 1883–1889, DOI: 10.1002/adfm.200800040.
6 S. Das, F. Pati, S. Chameettachal, S. Pahwa, A. R. Ray, S. Dhara and S. Ghosh, Enhanced redifferentiation of chondrocytes on microperiodic silk/gelatin scaffolds: toward tailor-made tissue engineering, *Biomacromolecules*, 2013, **14**(2), 311–321, DOI: 10.1021/bm301193t.
7 S. Chawla, A. Kumar, P. Admane, A. Bandyopadhyay and S. Ghosh, Elucidating role of silk-gelatin bioink to recapitulate articular cartilage differentiation in 3D bioprinted constructs, *Bioprinting*, 2017, **7**, 1–13, DOI: 10.1016/j.bprint.2017.05.001.
8 P. S. Yadav, M. P. Khan, P. Prashar, S. Duggal, S. K. Rath, N. Chattopadhyay and A. Bandyopadhyay, Characterization of BMP signaling dependent osteogenesis using a BMP depletable avianized bone marrow stromal cell line (TVA-BMSC), *Bone*, 2016, **91**, 39–52, DOI: 10.1016/j.bone.2016.07.010.
9 S. Ghosh, M. Laha, S. Mondal, S. Sengupta and D. L. Kaplan, In vitro model of mesenchymal condensation during

chondrogenic development, *Biomaterials*, 2009, **30**(33), 6530–6540, DOI: 10.1016/j.biomaterials.2009.08.019.

10 L. D. Koh, Y. Cheng, C. P. Teng, Y. W. Khin, X. J. Loh, S. Y. Tee, M. Low, E. Ye, H. D. Yu, Y. W. Zhang and M. Y. Han, Structures, mechanical properties and applications of silk fibroin materials, *Prog. Polym. Sci.*, 2015, **46**, 86–110, DOI: 10.1016/j.progpolymsci.2015.02.001.

11 M. McGill, J. M. Coburn, B. P. Partlow, X. Mu and D. Kaplan, Molecular and macro-scale analysis of enzyme-crosslinked silk hydrogels for rational biomaterial design, *Acta Biomater.*, 2017, **63**, 76–84, DOI: 10.1016/j.actbio.2017.09.020.

12 M. Basha, A. Aburub, F. F. Karageorgos, G. Tsoulfas and A. H. Alexopoulos, Advances in Gelatin-Based Tissue Engineering Using HRP/H_2O_2, *Gels*, 2025, **11**(6), 460, DOI: 10.3390/gels11060460.

13 F. Agostinacchio, V. Fitzpatrick, S. Dirè, D. L. Kaplan and A. Motta, Silk Fibroin-Based Inks for *in Situ* 3D Printing Using a Double Crosslinking Process, *Bioact. Mater.*, 2024, **35**, 122–134, DOI: 10.1016/j.bioactmat.2024.01.015.

14 T. Kotani, W. Mubarok, T. Hananouchi and S. Sakai, Horseradish peroxidase-mediated bioprinting via bioink gelation by alternately extruded support material, *ACS Biomater. Sci. Eng.*, 2023, **9**(10), 5804–5812, DOI: 10.1021/acsbiomaterials.3c00996.

15 F. Lee, J. E. Chung and M. Kurisawa, An Injectable Enzymatically Crosslinked Hyaluronic Acid–Tyramine Hydrogel System with Independent Tuning of Mechanical Strength and Gelation Rate, *Soft Matter*, 2008, **4**(4), 880–887, DOI: 10.1039/B719557E.

16 L. Andrée, P. Bertsch, R. Wang, M. Becker, J. Leijten, P. Fischer and S. C. Leeuwenburgh, A modular platform for cytocompatible hydrogels with tailored mechanical properties based on monolithic matrices and particulate building blocks, *Biomacromolecules*, 2023, **24**(6), 2755–2765, DOI: 10.1021/acs.biomac.3c00177.

17 A. M. Gardner, F. H. Xu, C. Fady, F. J. Jacoby, D. C. Duffey, Y. Tu and A. Lichtenstein, Apoptotic *vs.* nonapoptotic cytotoxicity induced by hydrogen peroxide, *Free Radicals Biol. Med.*, 1997, **22**(1–2), 73–83, DOI: 10.1016/s0891-5849(96)00235-3.

18 S. A. Bradner, B. P. Partlow, P. Cebe, F. G. Omenetto and D. L. Kaplan, Fabrication of elastomeric silk fibers, *Biopolymers*, 2017, **107**(9), e23030, DOI: 10.1002/bip.23030.

19 A. P. Tabatabai, B. P. Partlow, N. R. Raia, D. L. Kaplan and D. L. Blair, Silk molecular weight influences the kinetics of enzymatically cross-linked silk hydrogel formation, *Langmuir*, 2018, **34**(50), 15383–15387, DOI: 10.1021/acs.langmuir.8b02950.

20 S. Das, F. Pati, Y. J. Choi, G. Rijal, J. H. Shim, S. W. Kim, R. A. Ray, D. Woo Cho and S. Ghosh, Bioprintable, cell-laden silk fibroin–gelatin hydrogel supporting multilineage differentiation of stem cells for fabrication of three-dimensional tissue constructs, *Acta Biomater.*, 2015, **11**, 233–246, DOI: 10.1016/j.actbio.2014.09.023.

21 A. Sharma, G. Desando, M. Petretta, S. Chawla, I. Bartolotti, C. Manferdini, F. Paolella, E. Gabusi, D. Trucco, S. Ghosh and G. Lisignoli, Investigating the role of sustained calcium release in silk-gelatin-based three-dimensional bioprinted constructs for enhancing the osteogenic differentiation of human bone marrow derived mesenchymal stromal cells, *ACS Biomater. Sci. Eng.*, 2019, **5**(3), 1518–1533, DOI: 10.1021/acsbiomaterials.8b01631.

22 M. Haider, J. Cappello, H. Ghandehari and K. W. Leong, In Vitro Chondrogenesis of Mesenchymal Stem Cells in Recombinant Silk-Elastinlike Hydrogels, *Pharm. Res.*, 2007, **25**(3), 692, DOI: 10.1007/s11095-007-9282-8.

23 M. B. Mueller and R. S. Tuan, Functional characterization of hypertrophy in chondrogenesis of human mesenchymal stem cells, *Arthritis Rheum.*, 2008, **58**(5), 1377–1388, DOI: 10.1002/art.23370.

24 N. Majumder, C. Roy, L. Doenges, I. Martin, A. Barbero and S. Ghosh, Covalent Conjugation of Small Molecule Inhibitors and Growth Factors to a Silk Fibroin-Derived Bioink to Develop Phenotypically Stable 3D Bioprinted Cartilage, *ACS Appl. Mater. Interfaces*, 2024, **16**(8), 9925–9943, DOI: 10.1021/acsami.3c18903.

25 A. Schwab, R. Levato, M. D'Este, S. Piluso, D. Eglin and J. Malda, Printability and Shape Fidelity of Bioinks in 3D Bioprinting, *Chem. Rev.*, 2020, **120**(19), 11028–11055, DOI: 10.1021/acs.chemrev.0c00084.

26 D. N. Rockwood, R. C. Preda, T. Yücel, X. Wang, M. L. Lovett and D. L. Kaplan, Materials Fabrication from *Bombyx mori* Silk Fibroin, *Nat. Protoc.*, 2011, **6**(10), 1612–1631, DOI: 10.1038/nprot.2011.379.

27 P. De Stefano, F. Briatico-Vangosa, E. Bianchi, A. F. Pellegata, A. Hartung de Hartungen, P. Corti and G. Dubini, Bioprinting of matrigel scaffolds for cancer research, *Polymers*, 2021, **13**(12), 2026, DOI: 10.3390/polym13122026.

28 H. Park, X. Guo, J. S. Temenoff, Y. Tabata, A. I. Caplan, F. K. Kasper and A. G. Mikos, Effect of Swelling Ratio of Injectable Hydrogel Composites on Chondrogenic Differentiation of Encapsulated Rabbit Marrow Mesenchymal Stem Cells In Vitro, *Biomacromolecules*, 2009, **10**(3), 541, DOI: 10.1021/bm801197m.

29 K. A. Deo, K. A. Singh, C. W. Peak, D. L. Alge and A. K. Gaharwar, Bioprinting 101: Design, Fabrication, and Evaluation of Cell-Laden 3D Bioprinted Scaffolds, *Tissue Eng., Part A*, 2020, **26**(5–6), 318, DOI: 10.1089/ten.tea.2019.0298.

30 T. Zhang, W. Zhao, Z. Xiahou, X. Wang, K. Zhang and J. Yin, Bioink design for extrusion-based bioprinting, *Appl. Mater. Today*, 2021, **25**, 101227, DOI: 10.1016/j.apmt.2021.101227.

31 N. Majumder, A. Mishra and S. Ghosh, Effect of varying cell densities on the rheological properties of the bioink, *Bioprinting*, 2022, **28**, e00241, DOI: 10.1016/j.bprint.2022.e00241.

32 A. Sharma, P. Rawal, D. M. Tripathi, D. Alodiya, S. K. Sarin, S. Kaur and S. Ghosh, Upgrading hepatic differentiation and functions on 3D printed silk–decellularized liver hybrid scaffolds, *ACS Biomater. Sci. Eng.*, 2021, **7**(8), 3861–3873, DOI: 10.1021/acsbiomaterials.1c00671.

33 L. Yang, M. Jin, P. Du, G. Chen, C. Zhang, J. Wang, F. Jin, H. Shao, Y. She, S. Wang, L. Zheng and J. Wang, Study on Enhancement Principle and Stabilization for the Luminol-H_2O_2-HRP Chemiluminescence System, *PLoS One*, 2015, **10**(7), e0131193, DOI: 10.1371/journal.pone.0131193.

34 N. Majumder, S. Roy, A. Sharma, S. Arora, R. Vaishya, A. Bandyopadhyay and S. Ghosh, Assessing the Advantages of 3D Bioprinting and 3D Spheroids in Deciphering the Osteoarthritis Healing Mechanism Using Human Chondrocytes and Polarized Macrophages, *Biomed. Mater.*, 2024, **19**(2), 025005, DOI: 10.1088/1748-605X/ad1d18.

35 P. Admane, A. C. Gupta, P. Jois, S. Roy, C. C. Lakshmanan, G. Kalsi, B. Bandyopadhyay and S. Ghosh, Direct 3D bioprinted full-thickness skin constructs recapitulate regulatory signaling pathways and physiology of human skin, *Bioprinting*, 2019, **15**, e00051.

36 B. P. Partlow, C. W. Hanna, J. Rnjak-Kovacina, J. E. Moreau, M. B. Applegate, K. A. Burke and D. L. Kaplan, Highly tunable elastomeric silk biomaterials, *Adv. Funct. Mater.*, 2014, **24**(29), 4615–4624, DOI: 10.1002/adfm.201400526.

37 S. F. L. de Vries, P. K. J. Hanley and J. F. Welting, Chondrogenic Differentiation of Bone Marrow-Derived Mesenchymal Stem Cells: Tips and Tricks, *Methods Mol. Biol.*, 2011, **698**, 253–278, DOI: 10.1007/978-1-60761-999-4_20.

38 M. E. Cooke and D. H. Rosenzweig, The Rheology of Direct and Suspended Extrusion Bioprinting, *APL Bioeng.*, 2021, **5**(1), 011502, DOI: 10.1063/5.0031475.

39 M. Chopin-Doroteo, E. A. Mandujano-Tinoco and E. Krötzsch, Tailoring of the rheological properties of bioinks to improve bioprinting and bioassembly for tissue replacement, *Biochim. Biophys. Acta, Gen. Subj.*, 2021, **1865**(2), 129782, DOI: 10.1016/j.bbagen.2020.129782.

40 V. Kokol, Y. B. Pottathara, M. Mihelčič and L. S. Perše, Rheological Properties of Gelatine Hydrogels Affected by Flow- and Horizontally-Induced Cooling Rates during 3D Cryo-Printing, *Colloids Surf., A*, 2021, **616**, 126356, DOI: 10.1016/j.colsurfa.2021.126356.

41 R. Gutierrez-Contreras, M. Fernandez-Gutierrez, P. Olalla-Perez, A. De La Hoz and S. Marcos, Comparative analysis of silk fibroin membranes across cross-linking methods: processing and characterization, *ACS Omega*, 2024, **9**(37), 38452–38461, DOI: 10.1021/acsomega.4c02204.

42 J. K. Sahoo, J. Choi, O. Hasturk, I. Laubach, M. L. Descoteaux, S. Mosurkal, B. Wang, N. Zhang and D. L. Kaplan, Silk Degumming Time Controls Horseradish Peroxidase-Catalyzed Hydrogel Properties, *Biomater. Sci.*, 2020, **8**(15), 4176–4185, DOI: 10.1039/D0BM00512F.

43 P. I. Haris and F. Severcan, FTIR spectroscopic characterization of protein structure in aqueous and non-aqueous media, *J. Mol. Catal. B: Enzym.*, 1999, **7**(1–4), 207–221, DOI: 10.1016/S1381-1177(99)00030-2.

44 M. McGill, J. M. Grant and D. L. Kaplan, Enzyme-Mediated Conjugation of Peptides to Silk Fibroin for Facile Hydrogel Functionalization, *Ann. Biomed. Eng.*, 2020, **48**(7), 1905, DOI: 10.1007/s10439-020-02503-2.

45 A. Banerjee, M. Arha, S. Choudhary, R. S. Ashton, S. R. Bhatia, D. V. Schaffer and R. S. Kane, The influence of hydrogel modulus on the proliferation and differentiation of encapsulated neural stem cells, *Biomaterials*, 2009, **30**(27), 4695–4699, DOI: 10.1016/j.biomaterials.2009.05.050.

46 M. Temirel, S. R. Dabbagh and S. Tasoglu, Shape Fidelity Evaluation of Alginate-Based Hydrogels through Extrusion-Based Bioprinting, *J. Funct. Biomater.*, 2022, **13**(4), 225, DOI: 10.3390/jfb13040225.

47 N. Kuroda, K. Kawazoe, H. Nakano, M. Wada and K. Nakashima, New phenylboronic acid derivatives as enhancers of the luminol–H_2O_2–horseradish peroxidase chemiluminescence reaction, *Luminescence*, 1999, **14**(6), 361–364, DOI: 10.1002/(SICI)1522-7243(199911/12)14:6<361::AID-BIO563>3.0.CO;2-J.

48 J. Chakraborty, J. Fernández-Pérez, M. Takhsha Ghahfarokhi, K. A. van Kampen, T. ten Brink, J. Ramis, M. Kalogeropoulou, R. Cabassi, C. de Julián Fernández, F. Albertini, C. Mota, S. Ghosh and L. Moroni, Development of 4D-Bioprinted Shape-Morphing Magnetic Constructs for Cartilage Regeneration Using a Silk Fibroin-Gelatin Bioink, *Cell Rep. Phys. Sci.*, 2024, **5**(3), 101819, DOI: 10.1016/j.xcrp.2024.101819.

49 P. Taddei, V. Chiono, A. Anghileri, G. Vozzi, G. Freddi and G. Ciardelli, Silk Fibroin/G elatin Blend Films Crosslinked with Enzymes for Biomedical Applications, *Macromol. Biosci.*, 2013, **13**(11), 1492–1510, DOI: 10.1002/mabi.201300156.